SUPPORTING INFORMATION

Substitution Pattern Controlled Quantum Interference in [2.2]Paracyclophane-Based Single-Molecule Junctions

Ksenia Reznikova,†,# Chunwei Hsu,‡,# Werner M. Schosser,§,# Almudena Gallego,† Katawoura Beltako,§ Fabian Pauly,*,§ Herre S. J. van der Zant,*,‡ Marcel Mayor*,†,¶,¤

†Department of Chemistry, University of Basel, St. Johanns-Ring 19, 4056 Basel (Switzerland)

‡Kavli Institute of Nanoscience, Delft University of Technology, Lorentzweg 1, Delft 2628 CJ (The Netherlands)

§Institute of Physics, University of Augsburg, Universitätsstraße 1, 86159 Augsburg (Germany)

¶Institute for Nanotechnology, Karlsruhe Institute of Technology (KIT), P. O. Box 3640, 76021 Karlsruhe (Germany)

¤Lehn Institute of Functional Materials, School of Chemistry, Sun Yat-Sen University, Guangzhou 510274 (China)

*To whom correspondence should be addressed, Email: fabian.pauly@uni-a.de, h.s.j.vanderzant@tudelft.nl, marcel.mayor@unibas.ch

# These authors contributed equally to this work.

Table of Contents

1. Synthesis and Characterization

General Remarks: All commercially available compounds were purchased from Sigma-Aldrich, Acros, Apollo Scientific, Alfa Aesar, and Fluorochem and used without further purification. Anhydrous solvents were purchased from Sigma-Aldrich and stored over molecular sieves (4 Å). All reactions with reagents that are easily oxidized or hydrolyzed were performed under argon using *Schlenk* techniques with anhydrous solvents in oven-dried glassware. Column chromatography was performed on silica gel P60 (40-63 µm) from Silicycle™ using technical grade solvents. TLC was performed with silica gel 60 F254 aluminum sheets with a thickness of 0.25 mm purchased from Merck. Melting points were measured on a Büchi M-565 melting point apparatus and are uncorrected. ^{1}H-NMR and ^{13}C{^{1}H} NMR experiments were performed on Bruker Avance III NMR spectrometers operating at 500 MHz and 126 MHz proton frequencies, respectively. The instruments were equipped with an indirect-detection 5 mm BBI probe and with actively shielded z-gradients. The chemical shifts are reported in parts per million (ppm) referenced to the residual solvent peak, and the coupling constants (*J*) are given in hertz (Hz). All spectra were recorded at 298.15 K. For high-resolution mass spectra (HR-MS), a HR-ESI-ToF-MS measurement on a *maXis*™ 4G instrument from Bruker was used. Since the synthesized compounds **1a-4a** as well as **9-12** shown in this publication were less prone to form adducts with common ions like H^+, NH_4^+, K^+ or Na^+, the characteristic binding of silver ions to aromatic hydrocarbons[1,2] was used to increase the signal intensity in the HR-ESI-ToF-MS analysis.

1.1 Experimental Procedures

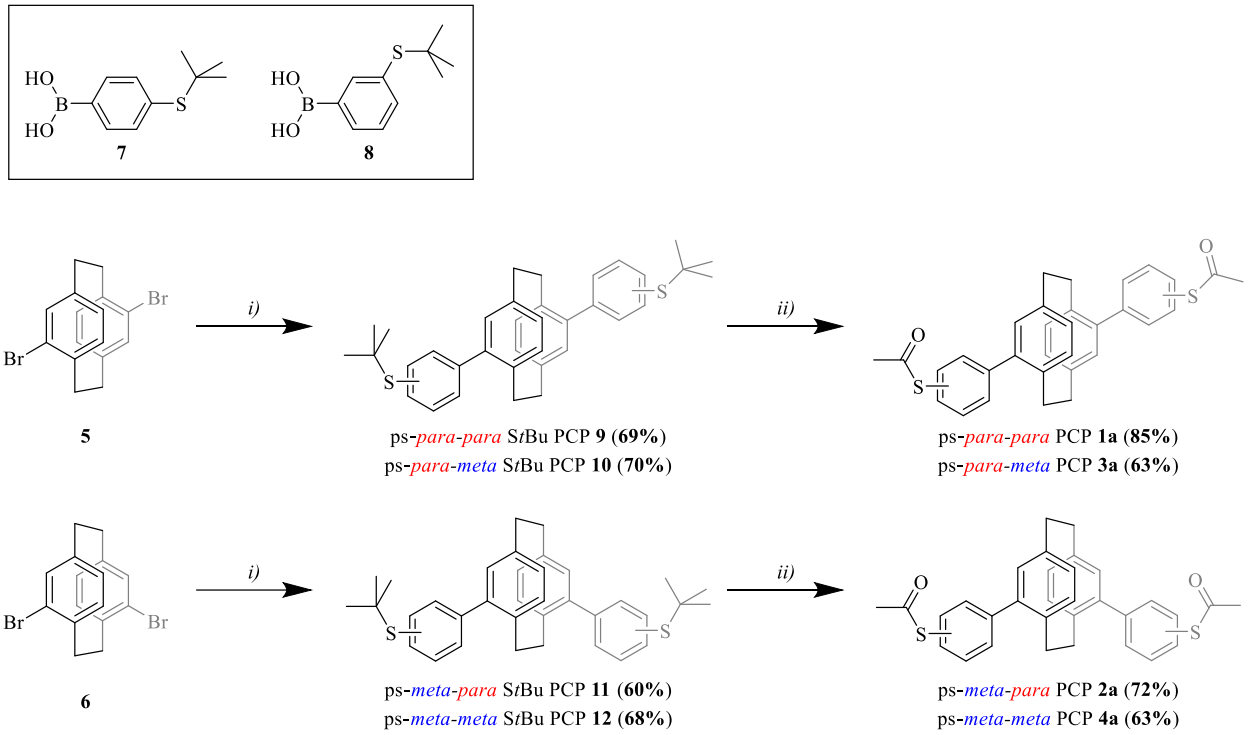

Scheme S1: Synthesis Overview: i) boronic acid **7** or **8**, K_2CO_3, $Pd(PPh_3)_4$, toluene/H_2O (6:1), 110 °C, 16 h; b) $Bi(OTf)_3$, AcCl, dry toluene/MeCN (1:1), RT, 2-3 h. The substitution patterns of the molecules in both the central PCP subunit and in the peripheral subunits are labeled in red and blue for *para*- and *meta*-substitution, respectively. For simplicity, the naming of structures was done according to the prefixes with ps as an abbreviation for pseudo, followed by the prefix referring to the substitution pattern of the central PCP subunit and the second one to the substitution pattern of the thiol anchoring group in the phenyl subunits.

Pseudo-*para*-dibromo[2.2]paracyclophane **5** and pseudo-*meta*-dibromo[2.2]paracyclophane **6** were synthesized over the bromination of [2.2]paracyclophane according to literature known procedure.[3] (3-(*Tert*-butylthio)phenyl)boronic acid **8** was commercially available. (4-(*Tert*-butylthio)phenyl)boronic acid **7** was prepared according to literature known procedures, starting from the respective 4-bromothiophenol and *tert*-butyl chloride in the presence of $AlCl_3$ to give the desired thioether[4], followed by lithium-halogen exchange, reacting with $B(OMe)_3$ and hydrolysis to the desired boronic acid **7**.[5]

General Procedure 1: *Suzuki* Cross-Coupling Reaction

Dibromo[2.2]paracyclophane **5** or **6** (1.0 eq.), boronic acid **7** or **8** (2.4 eq.), and potassium carbonate (2.0 eq.) were dissolved in toluene/water (6:1). The reaction mixture was sparged with argon for 20 min. $Pd(PPh_3)_4$ (10 mol%) was added, and the reaction mixture was heated to 110 °C for 16 h. Afterward, the reaction mixture was cooled to room temperature, diluted with toluene and washed with water (3x), brine (1x), dried over Na_2SO_4, and filtered. The solvent was removed under reduced pressure, and the crude product was purified by flash column chromatography.

General Procedure 2: Transprotection Reaction

This reaction procedure was adopted from literature.[6]

Previously prepared compounds **9** – **12** (1.0 eq.) and acetyl chloride (50 eq.) were dissolved in dry toluene/MeCN (1:1) under argon atmosphere. Bismuth(III)trifluoromethanesulfonate (3.0 eq.) was added and the reaction mixture was stirred at room temperature till full conversion was observed by TLC (2-3 h). Then, water was added, and the aqueous layer was extracted with CH_2Cl_2 (3x). The combined organic layers were dried over Na_2SO_4 and filtered. The solvent was removed under reduced pressure and the crude product was purified by flash column chromatography.

Pseudo-*para*-bis((4'-*tert*-butylthio)phenyl)[2.2]paracyclophane (ps-*para-para* S*t*Bu PCP 9):

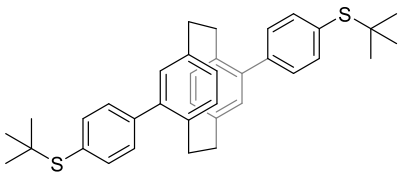

Compound **9** was synthesized according to general procedure 1 using pseudo-*para*-dibromo[2.2]paracyclophane **5** (200 mg, 546 µmol, 1.0 eq.), (4-(*tert*-butylthio)phenyl)boronic acid **7** (275 mg, 1.31 mmol, 2.4 eq.), K_2CO_3 (151 mg, 1.09 mmol, 2.0 eq.), $Pd(PPh_3)_4$ (63 mg, 54.6 µmol, 10 mol%), toluene (12 mL) and water (2 mL). The crude was purified by flash column chromatography (cyclohexane/CH_2Cl_2 2:1) to give ps-*para-para* S*t*Bu PCP **9** (201 mg, 386 µmol, 69%) as a white solid.

TLC (SiO_2, cyclohexane/CH_2Cl_2 2:1): R_f =0.15

m.p. > 270 °C (decomposition)

^{1}H NMR (500 MHz, $CDCl_3$): δ 7.68 – 7.62 (m, 4H, Ar-H), 7.51 – 7.47 (m, 4H, Ar-H), 6.69 – 6.64 (m, 4H, PCPAr-H), 6.60 (dd, *J* = 7.7, 1.9 Hz, 2H, PCPAr-H), 3.45 (ddd, *J* = 13.9, 9.9, 4.3 Hz, 2H, CH_2), 3.04 (ddd, *J* = 13.9, 10.0, 4.7 Hz, 2H, CH_2), 2.87 (ddd, *J* = 14.1, 10.0, 4.2 Hz, 2H, CH_2), 2.78 (ddd, *J* = 13.7, 9.9, 4.7 Hz, 2H, CH_2), 1.36 (s, 18H, *t*Bu-H) ppm.

^{13}C{^{1}H} NMR (126 MHz, $CDCl_3$): δ 141.8, 141.5, 140.1, 137.7, 137.0, 135.0, 132.5, 131.4, 129.9, 129.6, 46.2, 34.9, 34.0, 31.2 ppm.

HR-MS (ESI, +): *m/z* calcd. for $C_{36}H_{40}S_2Ag$ $[M+Ag]^+$ 643.1617; found: 643.1604.

Pseudo-*para*-bis((4'-acetylthio)phenyl)[2.2]paracyclophane (ps-*para-para* PCP 1a):

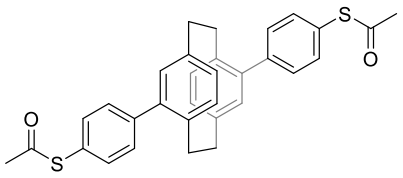

Compound **1a** was synthesized according to general procedure 2 using compound **9** (51 mg, 95 µmol, 1.0 eq.), acetyl chloride (0.34 mL, 4.75 mmol, 50 eq.), bismuth(III)trifluoromethane-sulfonate (189 mg, 282 µmol, 3.0 eq.), toluene (10 mL) and acetonitrile (10 mL). The crude was purified by flash column chromatography (cyclohexane/CH_2Cl_2 1:4) to give ps-*para-para* PCP **1a** (41 mg, 81 µmol, 85%) as a white solid.

TLC (SiO_2, cyclohexane/CH_2Cl_2 1:4): R_f =0.19

m.p. > 290 °C (decomposition)

^{1}H NMR (500 MHz, $CDCl_3$): 7.59 – 7.52 (m, 8H, Ar-H), 6.68 – 6.64 (m, 4H, PCPAr-H), 6.59 (dd, *J* = 7.8, 1.9 Hz, 2H, PCPAr-H), 3.44 (ddd, *J* = 14.0, 9.9, 4.4 Hz, 2H, CH_2), 3.05 (ddd, *J* = 14.0, 9.9, 4.8 Hz, 2H, CH_2), 2.90 – 2.78 (m, 4H, CH_2), 2.48 (s, 6H, SAc-H) ppm.

^{13}C{^{1}H} NMR (126 MHz, $CDCl_3$): δ 194.2, 142.5, 141.2, 140.2, 137.1, 135.1, 134.6, 132.5, 130.6, 129.8, 126.6, 34.9, 33.9, 30.4 ppm.

HR-MS (ESI, +): *m/z* calcd. for $C_{32}H_{28}O_2S_2Ag$ $[M+Ag]^+$ 615.0576; found: 615.0572.

Pseudo-*para*-bis((3'-*tert*-butylthio)phenyl)[2.2]paracyclophane (ps-*para-meta* S*t*Bu PCP 10):

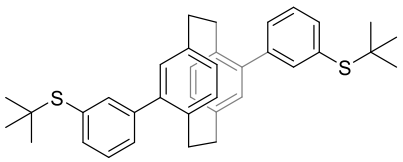

Compound **10** was synthesized according to general procedure 1 using pseudo-*para*-dibromo[2.2]paracyclophane **5** (150 mg, 410 µmol, 1.0 eq.), (3-(*tert*-butylthio)phenyl)boronic acid **8** (207 mg, 984 µmol, 2.4 eq.), K_2CO_3 (113 mg, 820 µmol, 2.0 eq.), $Pd(PPh_3)_4$ (47 mg, 41 µmol, 10 mol%), toluene (12 mL) and water (2 mL). The crude was purified by flash column chromatography (cyclohexane/CH_2Cl_2 3:1) to give ps-*para-meta* S*t*Bu PCP **10** (154 mg, 287 µmol, 70%) as a white solid.

TLC (SiO_2, cyclohexane/CH_2Cl_2 3:1): R_f =0.15

m.p.: 168 – 170 °C

^{1}H NMR (500 MHz, $CDCl_3$): δ 7.72 (t, *J* = 1.7 Hz, 2H, Ar-H), 7.55 (m, 4H, Ar-H), 7.46 (t, *J* = 7.6 Hz, 2H, Ar-H), 6.69 – 6.66 (m, 4H, PCPAr-H), 6.60 (dd, *J* = 7.9, 1.9 Hz, 2H, PCPAr-H), 3.45 (ddd, *J* = 13.9, 10.0, 4.3 Hz, 2H, CH_2), 3.05 (ddd, *J* = 14.0, 10.0, 4.7 Hz, 2H, CH_2), 2.87 (ddd, *J* = 14.1, 10.0, 4.3 Hz, 2H, CH_2), 2.79 (ddd, *J* = 13.7, 9.9, 4.7 Hz, 2H, CH_2), 1.38 (s, 18H, *t*Bu-H) ppm.

^{13}C{^{1}H} NMR (126 MHz, $CDCl_3$): δ 141.7, 141.5, 140.1, 138.9, 137.0, 136.0, 135.0, 133.0, 132.4, 130.4, 129.5, 128.8, 46.3, 34.9, 33.9, 31.2 ppm.

HR-MS (ESI, +): *m/z* calcd. for $C_{36}H_{40}S_2Ag$ $[M+Ag]^+$ 643.1617; found: 643.1610.

Pseudo-*para*-bis((3'-acetylthio)phenyl)[2.2]paracyclophane (ps-*para-meta* PCP 3a):

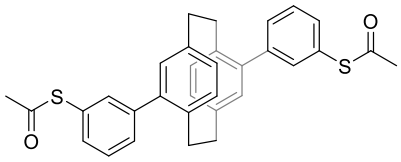

Compound **3a** was synthesized according to general procedure 2 using compound **10** (50 mg, 93.1 µmol, 1.0 eq.), acetyl chloride (0.33 mL, 4.66 mmol, 50 eq.), bismuth(III)trifluoromethanesulfonate (187 mg, 279 µmol, 3.0 eq.), toluene (4 mL) and acetonitrile (4 mL). The crude was purified by flash column chromatography (cyclohexane/CH_2Cl_2 1:2) to give ps-*para-meta* PCP **3a** (30 mg, 59 µmol, 63%) as a white amorphous solid.

TLC (SiO_2, cyclohexane/CH_2Cl_2 1:2): R_f =0.15

^{1}H NMR (500 MHz, $CDCl_3$): δ 7.59 – 7.56 (m, 4H, Ar-H), 7.54 (t, *J* = 7.8 Hz, 2H, Ar-H), 7.43 (dt, *J* = 7.4, 1.6 Hz, 2H, Ar-H), 6.67 – 6.62 (m, 6H, PCPAr-H), 3.48 (ddd, *J* = 13.8, 9.9, 4.2 Hz, 2H, CH_2), 3.04 (ddd, *J* = 14.0, 10.0, 4.9 Hz, 2H, CH_2), 2.92 – 2.78 (m, 4H, CH_2), 2.49 (s, 6H, SAc-H) ppm.

^{13}C{^{1}H} NMR (126 MHz, $CDCl_3$): δ 194.0, 142.4, 141.1, 140.2, 137.1, 136.0, 135.0, 132.5, 132.4, 130.9, 129.7, 129.5, 128.3, 34.8, 33.8, 30.5 ppm.

HR-MS (ESI, +): *m/z* calcd. for $C_{32}H_{28}O_2S_2Ag$ $[M+Ag]^+$ 615.0576; found: 615.0576.

Pseudo-*meta*-bis((4'-*tert*-butylthio)phenyl)[2.2]paracyclophane (ps-*meta-para* S*t*Bu PCP 11):

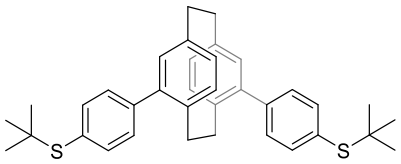

Compound **11** was synthesized according to general procedure 2 using pseudo-*meta*-dibromo[2.2]paracyclophane **6** (200 mg, 546 µmol, 1.0 eq.), (4-(*tert*-butylthio)phenyl)boronic acid **7** (275 mg, 1.31 mmol, 2.4 eq.), K_2CO_3 (151 mg, 1.09 mmol, 2.0 eq.), $Pd(PPh_3)_4$ (63 mg, 54 µmol, 2.0 eq.), toluene (12 mL) and water (2 mL). The crude was purified by flash column chromatography (cyclohexane/CH_2Cl_2 3:1). The remaining impurities were precipitating in CH_2Cl_2 by adding MeOH, followed by filtration and evaporation of mother liquor to give ps-*meta-para* PCP **11** (175 mg, 344 µmol, 60%) as a colorless oil.

TLC (SiO_2, cyclohexane/CH_2Cl_2 2:1): R_f =0.23

^{1}H NMR (500 MHz, $CDCl_3$): δ 7.65 – 7.61 (m, 4H, Ar-H), 7.48 – 7.44 (m, 4H, Ar-H), 6.72 (d, *J* = 1.9 Hz, 2H, PCPAr-H), 6.69 (d, *J* = 7.8 Hz, 2H, PCPAr-H), 6.58 (dd, *J* = 7.7, 1.9 Hz, 2H, PCPAr-H), 3.28 – 3.06 (m, 6H, CH_2), 2.56 – 2.48 (m, 2H, CH_2), 1.35 (s, 18H, *t*Bu-H) ppm.

^{13}C{^{1}H} NMR (126 MHz, $CDCl_3$): δ 141.9, 141.6, 139.8, 137.7, 137.5, 132.5, 132.0, 131.6, 131.4, 129.8, 46.2, 35.3, 33.6, 31.2 ppm.

HR-MS (ESI, +): *m/z* calcd. for $C_{36}H_{40}AgS_2$ $[M+Ag]^+$ 643.1617; found: 643.1615.

Pseudo-*meta*-bis((4'-*tert*-acetylthio)phenyl)[2.2]paracyclophane (ps-*meta-para* PCP 2a):

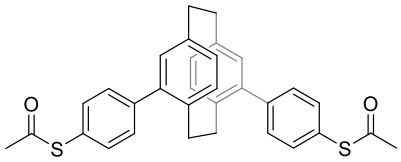

Compound **2a** was synthesized according to general procedure 2 using compound **11** (20 mg, 37.3 µmol, 1.0 eq.), acetyl chloride (0.13 mL, 1.86 mmol, 50 eq.), bismuth(III)trifluoromethanesulfonate (74.9 mg, 112 µmol, 3.0 eq.), toluene (2 mL) and acetonitrile (2 mL). The crude was purified by flash column chromatography (cyclohexane/CH_2Cl_2 1:2) to give ps-*meta-para* PCP **2a** (13.6 mg, 33 µmol, 72%) as a white amorphous solid.

TLC (SiO_2, cyclohexane/CH_2Cl_2 1:2): R_f =0.32

^{1}H NMR (500 MHz, $CDCl_3$): δ 7.54 – 7.50 (m, 8H, Ar-H), 6.72 (d, *J* = 1.9 Hz, 2H, PCPAr-H), 6.67 (d, *J* = 7.9 Hz, 2H, PCPAr-H), 6.57 (dd, *J* = 7.8, 1.9 Hz, 2H, PCPAr-H), 3.27 – 3.07 (m, 4H, CH_2), 2.62 – 2.54 (m, 2H, CH_2), 2.47 (s, 6H, SAc-H) ppm.

^{13}C{^{1}H} NMR (126 MHz, $CDCl_3$): δ 194.2, 142.4, 141.7, 139.9, 137.6, 134.6, 132.6, 132.1, 131.8, 130.5, 126.6, 35.3, 33.5, 30.4 ppm.

HR-MS (ESI, +): *m/z* calcd. for $C_{32}H_{28}O_2S_2Ag$ $[M+Ag]^+$ 615.0576; found: 615.0583.

Pseudo-*meta*-bis((3'-*tert*-butylthio)phenyl)[2.2]paracyclophane (ps-*meta-meta* S*t*Bu PCP 12):

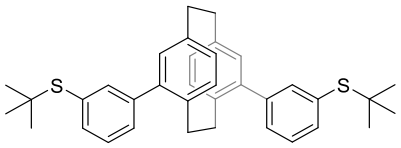

Compound **12** was synthesized according to general procedure 2 using pseudo-*meta*-dibromo[2.2]paracyclophane **6** (150 mg, 410 µmol, 1.0 eq.), (3-(*tert*-butylthio)phenyl)boronic acid **8** (200 mg, 952 µmol, 2.4 eq.), K_2CO_3 (113 mg, 820 µmol, 2.0 eq.), $Pd(PPh_3)_4$ (47.4 mg, 41 µmol, 10 mol%), toluene (12 mL) and water (2 mL). The crude was purified by flash column chromatography (cyclohexane/CH_2Cl_2 4:1). The remaining impurities were precipitating in CH_2Cl_2 by adding MeOH, followed by filtration and evaporation of mother liquor to give ps-*meta-meta* S*t*Bu PCP **12** (149 mg, 278 kµmol, 68 %) as a colorless oil.

TLC (SiO_2, cyclohexane/CH_2Cl_2 4:1): R_f =0.13

^{1}H NMR (500 MHz, $CDCl_3$): δ 7.68 (t, *J* = 1.7 Hz, 2H, Ar-H), 7.54 (dt, *J* = 7.5, 1.5 Hz, 2H, Ar-H), 7.49 (dt, *J* = 7.7, 1.5 Hz, 2H, Ar-H), 7.44 (t, *J* = 7.6 Hz, 2H, Ar-H), 6.72 (d, *J* = 1.9 Hz, 2H, PCPAr-H), 6.68 (d, *J* = 7.8 Hz, 2H, PCPAr-H), 6.59 (dd, *J* = 7.8, 1.9 Hz, 2H, PCPAr-H), 3.27 – 3.06 (m, 6H, CH_2), 2.58 – 2.49 (m, 2H, CH_2), 1.36 (s, 18H, *t*Bu-H) ppm.

^{13}C{^{1}H} NMR (126 MHz, $CDCl_3$): δ 141.9, 141.6, 139.9, 138.7, 137.5, 136.0, 133.0, 132.4, 132.0, 131.6, 130.2, 128.8, 46.3, 35.3, 33.6, 31.2 ppm.

HR-MS (ESI, +): *m/z* calcd. for $C_{36}H_{40}AgS_2$ $[M+Ag]^+$ 643.1617; found: 643.1604.

Pseudo-*meta*-bis((3'-*tert*-acetylthio)phenyl)[2.2]paracyclophane (ps-*meta-meta* PCP 4a):

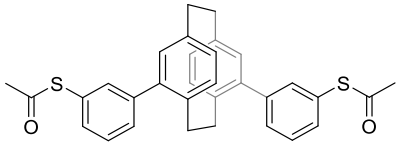

Compound **4a** was synthesized according to general procedure 2 using compound **12** (50 mg, 93.1 µmol, 1.0 eq.), acetyl chloride (0.33 mL, 4.66 mmol, 50 eq.), bismuth(III)trifluoromethanesulfonate (187 mg, 279 µmol, 3.0 eq.), toluene (4 mL) and acetonitrile (4 mL). The crude was purified by flash column chromatography (cyclohexane/CH_2Cl_2 1:2) to give ps-*meta-meta* PCP **4a** (31 mg, 61 µmol, 66%) as a white amorphous solid.

TLC (SiO_2, cyclohexane/CH_2Cl_2 1:2): R_f=0.26

^{1}H NMR (500 MHz, $CDCl_3$): δ 7.56 – 7.49 (m, 6H, Ar-H), 7.41 (dt, *J* = 6.7, 1.9 Hz, 2H, Ar-H), 6.73 (d, *J* = 7.8 Hz, 2H, PCPAr-H), 6.69 (d, *J* = 1.9 Hz, 2H, PCPAr-H), 6.58 (dd, *J* = 7.8, 1.9 Hz, 2H, PCPAr-H), 3.27 – 3.16 (m, 4H, CH_2), 3.14 – 3.06 (m, 2H, CH_2), 2.60 – 2.51 (m, 2H, CH_2), 2.47 (s, 6H, SAc-H) ppm.

^{13}C{^{1}H} NMR (126 MHz, $CDCl_3$): δ 194.0, 142.2, 141.5, 139.8, 137.7, 135.7, 132.6, 132.5, 132.0, 131.7, 130.8, 129.5, 128.3, 35.2, 33.5, 30.5 ppm.

HR-MS (ESI, +): *m/z* calcd. for $C_{32}H_{28}O_2S_2Ag$ $[M+Ag]^+$ 615.0576; found: 615.0577.

1.2 Characterization

^{1}H, $^{13}C\{^{1}H\}$ NMR ($CDCl_3$, 500/126 MHz) and HR-MS spectra of ps-*para-para* S*t*Bu PCP (9)

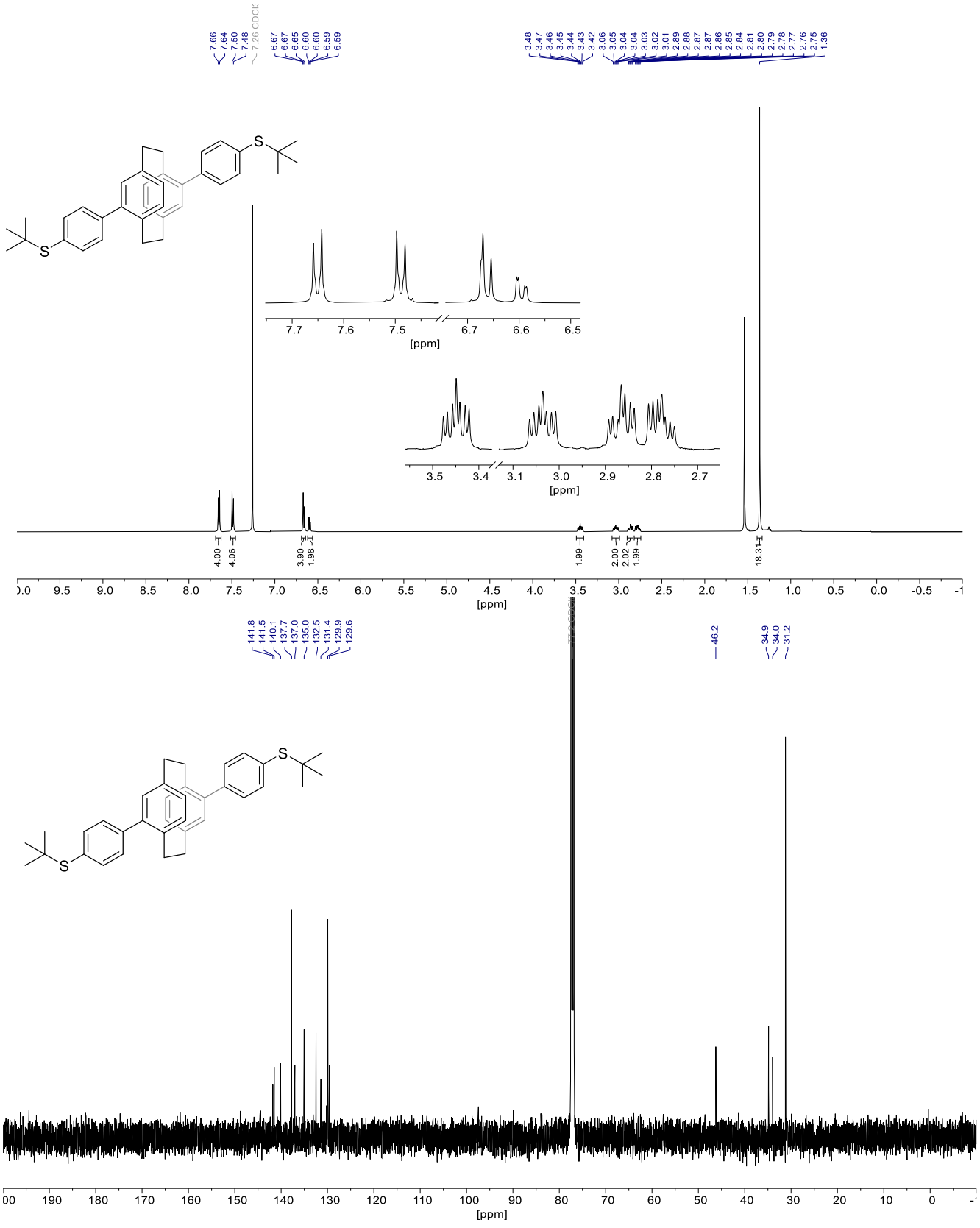

High Resolution Mass Spectrometry Report

Sample Name	**KR-262**	Instrument	maXis 4G
Comment	in MeOH+ AgNO3 (1mM)	Method	22 Direct_pos_mid.m

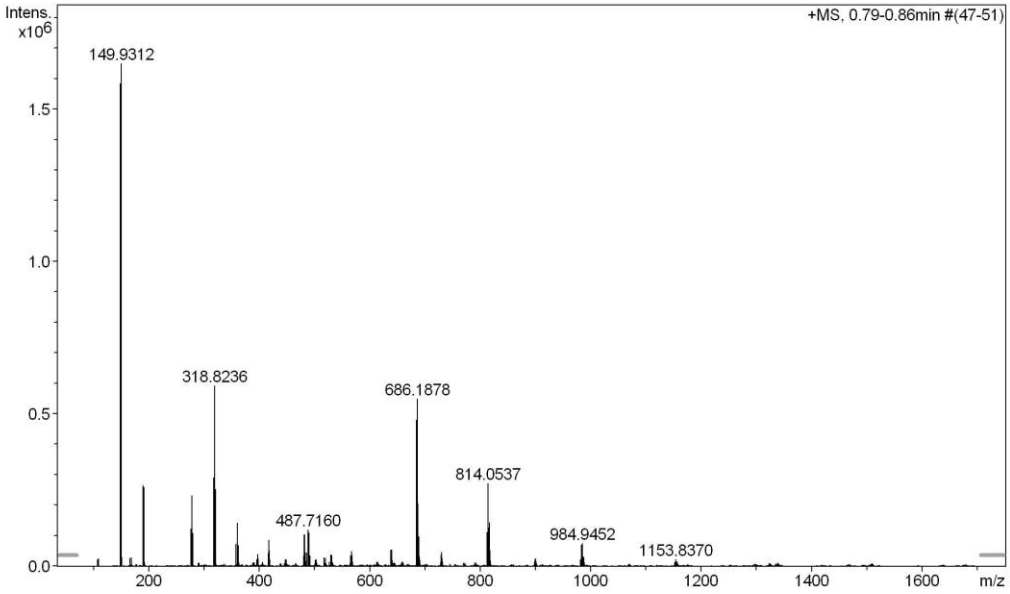

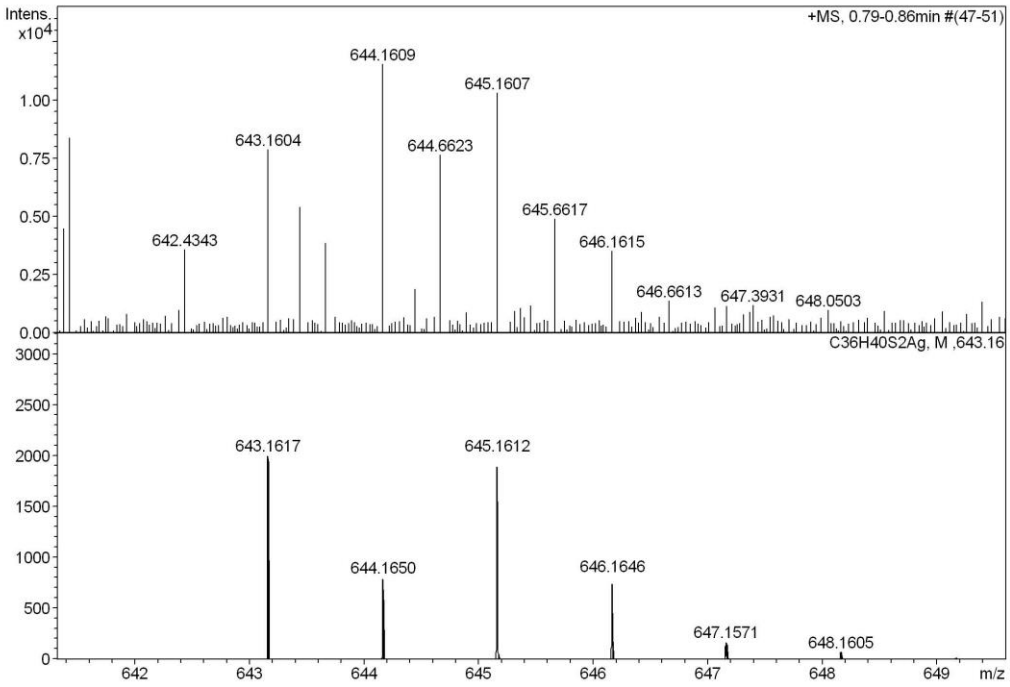

High Resolution Mass Spectrometry Report

Measured m/z vs. theoretical m/z

Meas. m/z	#	Formula	Score	m/z	err [mDa]	err [ppm]	mSigma	rdb	e^- Conf	z
643.1604	1	C 36 H 40 Ag S 2	100.00	643.1617	1.3	2.0	258.3	16.5	even	1+

Mass list

#	m/z	I %	I
1	106.9052	1.2	20279
2	108.9048	1.4	23458
3	147.9315	96.0	1581629
4	148.9343	1.6	26334
5	149.9312	100.0	1647778
6	150.9339	1.7	28649
7	165.9418	1.6	25731
8	167.9415	1.7	27880
9	188.9575	16.0	263703
10	189.9602	0.8	13354
11	190.9572	15.6	257458
12	275.7969	7.4	121156
13	277.7967	14.0	230062
14	279.7962	6.5	107139
15	316.8237	17.6	290533
16	318.8236	35.9	591526
17	320.8230	15.2	250711
18	357.8499	4.4	72285
19	359.8499	8.6	141120
20	361.8494	4.1	66776
21	395.5457	1.3	20663
22	396.5457	2.4	39104
23	397.0472	1.1	18085
24	397.5456	1.5	24121
25	405.5510	0.8	13571
26	416.0588	2.5	41310
27	416.5606	1.2	19402
28	417.0589	5.1	84232
29	417.5602	2.4	38866
30	418.0588	3.0	50053
31	418.5600	1.3	21243
32	446.6891	1.3	21215
33	448.6888	1.2	20346
34	479.9921	2.1	33840
35	480.4938	0.9	14740
36	480.9922	6.2	102317
37	481.4935	2.7	44129
38	481.9921	6.2	101927
39	482.4933	2.7	44896
40	482.9919	2.6	42563
41	483.4932	1.0	16473
42	485.7161	2.6	43245
43	487.7160	7.2	117873
44	489.7158	6.6	108685
45	491.7152	2.0	33477
46	501.5051	1.2	19699
47	502.5052	1.2	20438
48	517.2947	1.6	26448
49	519.2945	1.6	25673
50	526.7423	0.8	13289
51	528.7423	2.2	37020
52	530.7422	2.1	34571
53	565.4383	2.0	33729
54	565.9395	0.9	14453
55	566.4384	3.0	48686
56	566.9396	1.3	22132
57	567.4383	2.2	35497
58	567.9397	0.9	14124
59	612.4247	0.8	13127
60	637.3733	3.2	53324
61	638.3763	1.3	20631
62	639.3734	3.2	52899

High Resolution Mass Spectrometry Report

#	m/z	I %	I
63	640.3765	1.2	19479
64	658.6079	0.8	13811
65	684.1878	29.0	478559
66	685.1907	11.7	192316
67	686.1878	33.2	547250
68	687.1903	12.4	205018
69	688.1882	5.8	95824
70	689.1889	1.8	29673
71	690.1874	1.2	19446
72	728.6070	2.2	35542
73	729.1084	1.8	29596
74	729.6072	2.7	45273
75	730.1081	1.9	31479
76	730.6076	1.5	25081
77	731.1080	0.9	14453
78	812.0534	6.7	110291
79	813.0553	4.1	67761
80	813.5548	1.4	22506
81	814.0537	16.4	270196
82	814.5546	2.0	33543
83	815.0555	7.5	124269
84	815.5542	1.5	25068
85	816.0535	8.6	141865
86	817.0554	3.1	50592
87	818.0534	1.0	16277
88	898.4994	1.3	20785
89	899.0009	1.0	16009
90	899.4999	1.4	23565
91	900.0006	1.0	16252
92	900.5002	0.9	15574
93	980.9450	1.3	21169
94	982.9453	4.2	68581
95	983.9475	2.2	35753
96	984.9452	4.5	73890
97	985.9476	1.8	30258
98	986.9451	1.6	27076
99	1153.8370	1.2	20362
100	1155.8374	0.9	14825

Acquisition Parameter

General	Fore Vacuum	2.48e+000 mBar	High Vacuum	1.14e-007 mBar	Source Type	ESI
	Scan Begin	75 m/z	Scan End	1700 m/z	Ion Polarity	Positive
Source	Set Nebulizer	0.4 Bar	Set Capillary	3600 V	Set Dry Gas	4.0 l/min
	Set Dry Heater	180 °C	Set End Plate Offset	-500 V		
Quadrupole	Set Ion Energy (MS only)	4.0 eV				
Coll. Cell	Collision Energy	8.0 eV	Set Collision Cell RF	350.0 Vpp	100.0 Vpp	
Ion Cooler	Set Ion Cooler Transfer Time	75.0 µs	Set Ion Cooler Pre Pulse Storage Time	10.0 µs		

^{1}H, ^{13}C{^{1}H} NMR ($CDCl_3$, 500/126 MHz) and HR-MS spectra of ps-*para-para* PCP (1a)

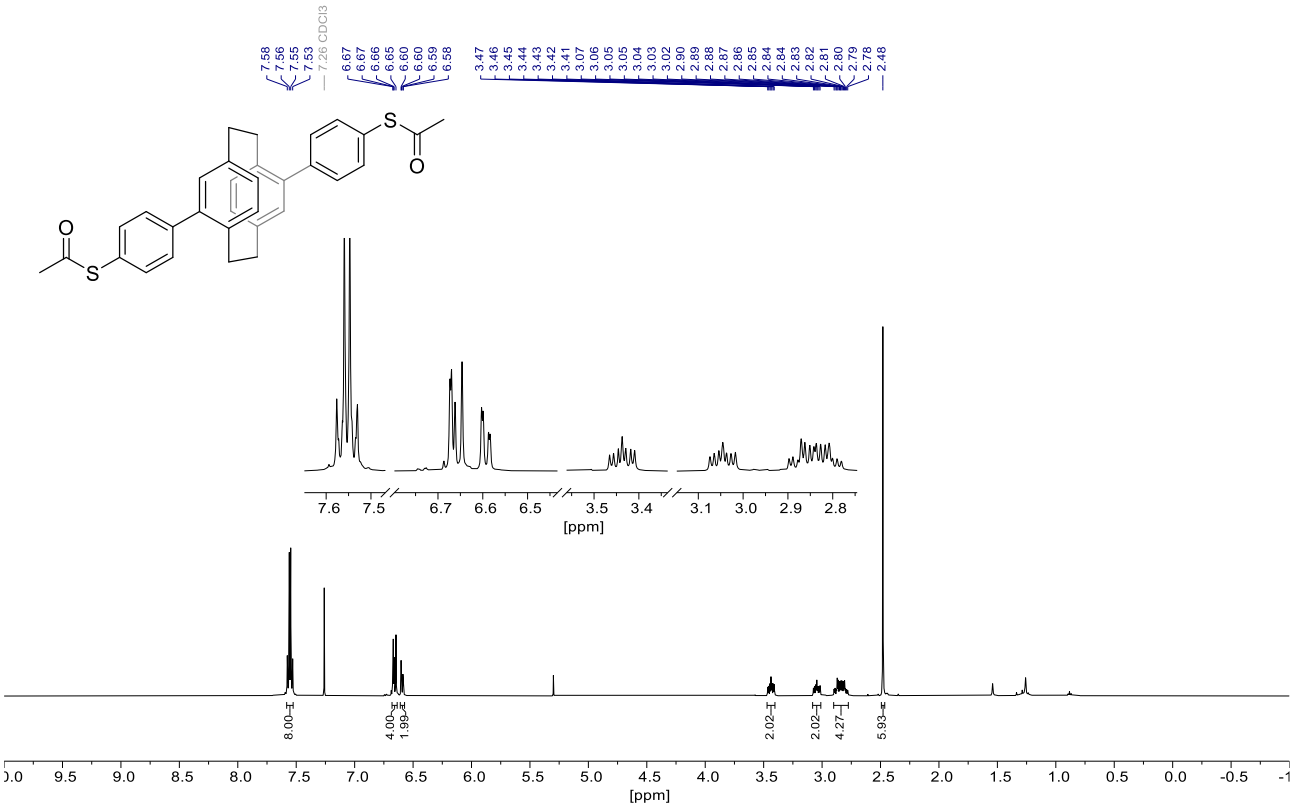

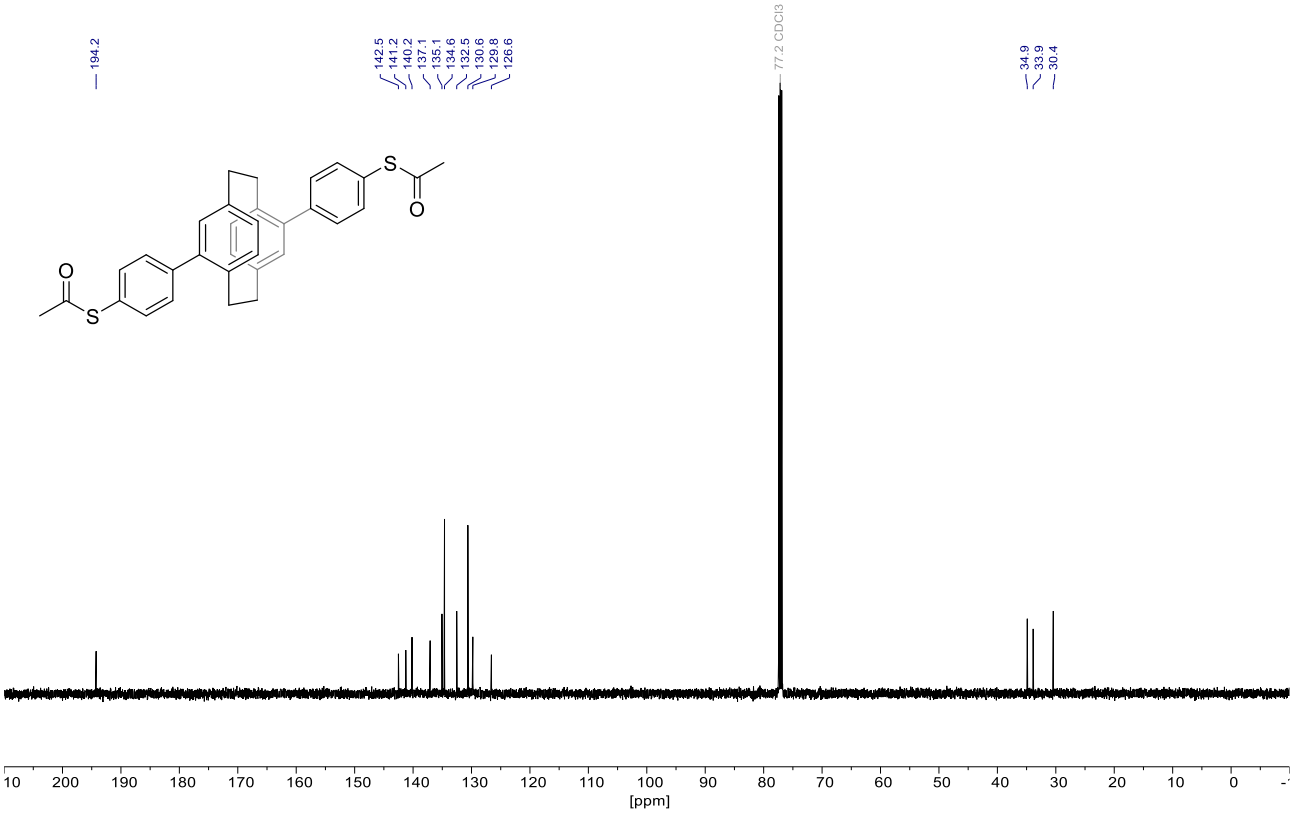

High Resolution Mass Spectrometry Report

Sample Name **KR-263**
Comment in MeOH+ AgNO3 (1mM)

Instrument maXis 4G
Method 22 Direct_pos_mid.m

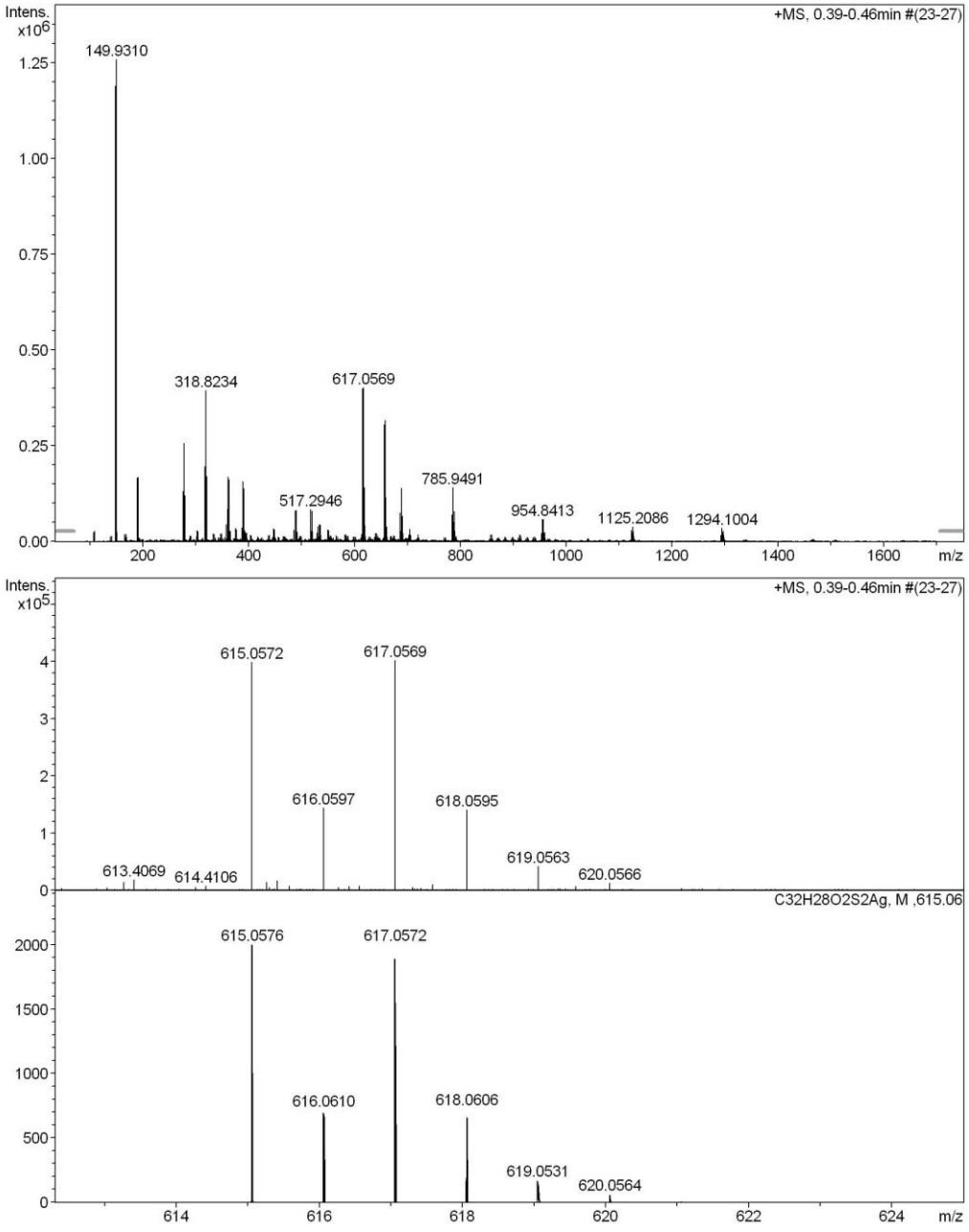

High Resolution Mass Spectrometry Report

Measured m/z vs. theoretical m/z

Meas. m/z	#	Formula	Score	m/z	err [mDa]	err [ppm]	mSigma	rdb	e⁻ Conf	z
615.0572	1	C 32 H 28 Ag O 2 S 2	100.00	615.0576	0.4	0.7	32.6	18.5	even	1+

Mass list

#	m/z	I %	I
1	106.9050	1.9	23660
2	108.9047	2.2	27107
3	147.9313	94.4	1187570
4	148.9341	1.6	20441
5	149.9310	100.0	1257418
6	150.9336	1.9	24031
7	165.9417	1.5	18271
8	167.9414	1.4	18231
9	188.9573	13.2	165848
10	190.9570	13.2	166362
11	275.7968	10.4	130154
12	277.7966	20.3	255627
13	279.7961	9.5	119021
14	301.9602	2.2	27662
15	303.9597	2.1	26151
16	316.8234	15.5	194421
17	318.8234	31.3	393288
18	320.8227	13.4	169063
19	333.0967	1.5	19119
20	335.0968	1.5	18864
21	347.1123	1.6	19538
22	349.1124	1.5	19008
23	357.8497	3.4	43273
24	359.8495	6.7	83930
25	361.1284	13.4	168196
26	361.8491	3.2	40623
27	362.1314	2.4	30025
28	363.1283	12.8	160916
29	364.1313	2.1	26811
30	365.1430	2.1	26027
31	375.1436	2.7	33855
32	377.1435	2.4	30415
33	387.1435	2.8	34911
34	389.1592	12.4	156450
35	390.1626	2.3	29459
36	391.1595	10.9	137667
37	392.1627	2.3	28500
38	394.1494	1.8	22241
39	396.1492	1.7	21480
40	446.6889	2.6	32334
41	448.6886	2.4	30221
42	485.7158	2.4	29742
43	487.7157	6.4	80979
44	489.7153	6.4	79962
45	491.7148	1.9	24464
46	517.2946	6.6	82573
47	518.2978	2.2	27284
48	519.2945	6.3	79621
49	520.2973	2.1	26123
50	528.7421	1.7	21944
51	530.7417	1.7	21017
52	531.2588	3.1	39050
53	533.2590	3.1	39554
54	533.2885	3.5	44438
55	534.2902	1.3	16864
56	535.2891	3.4	42412
57	549.2845	2.5	31056
58	551.2844	2.2	27751
59	581.2738	1.4	17629
60	583.2738	1.3	16908
61	613.4069	1.4	18135
62	615.0572	31.7	397975

High Resolution Mass Spectrometry Report

#	m/z	I %	I
63	616.0597	11.4	143376
64	617.0569	31.9	400812
65	618.0595	11.2	140297
66	619.0563	3.3	41228
67	639.4242	1.7	21173
68	641.4300	1.6	20709
69	656.0835	24.3	304927
70	657.0861	8.8	110302
71	658.0834	25.1	315449
72	659.0858	9.1	114072
73	660.0834	3.0	38024
74	686.1875	5.9	74801
75	687.1904	2.1	26466
76	688.1876	11.1	139410
77	689.1900	3.7	46245
78	690.1875	5.2	65533
79	691.1900	1.7	21000
80	704.1818	2.5	31264
81	783.9490	5.5	69485
82	784.9517	2.1	26566
83	785.9491	11.1	139938
84	786.9515	4.0	49781
85	787.9487	6.2	78496
86	788.9512	2.2	27129
87	857.0797	1.4	17593
88	952.8408	1.6	20109
89	954.8413	4.6	57478
90	955.8442	1.7	21908
91	956.8412	4.6	57220
92	957.8440	1.7	21398
93	958.8405	1.8	22896
94	1123.2074	2.3	29368
95	1124.2112	1.7	21832
96	1125.2086	3.0	38040
97	1126.2109	2.0	25531
98	1294.1004	2.8	34667
99	1295.1035	1.9	23566
100	1296.1016	2.1	26333

Acquisition Parameter

General	Fore Vacuum	2.48e+000 mBar	High Vacuum	1.14e-007 mBar	Source Type	ESI
	Scan Begin	75 m/z	Scan End	1700 m/z	Ion Polarity	Positive
Source	Set Nebulizer	0.4 Bar	Set Capillary	3600 V	Set Dry Gas	4.0 l/min
	Set Dry Heater	180 °C	Set End Plate Offset	-500 V		
Quadrupole	Set Ion Energy (MS only)	4.0 eV				
Coll. Cell	Collision Energy	8.0 eV	Set Collision Cell RF	350.0 Vpp	100.0 Vpp	
Ion Cooler	Set Ion Cooler Transfer Time	75.0 µs	Set Ion Cooler Pre Pulse Storage Time	10.0 µs		

^{1}H, ^{13}C{^{1}H} NMR ($CDCl_3$, 500/126 MHz) and HR-MS spectra of ps-*para-meta* S*t*Bu PCP (10)

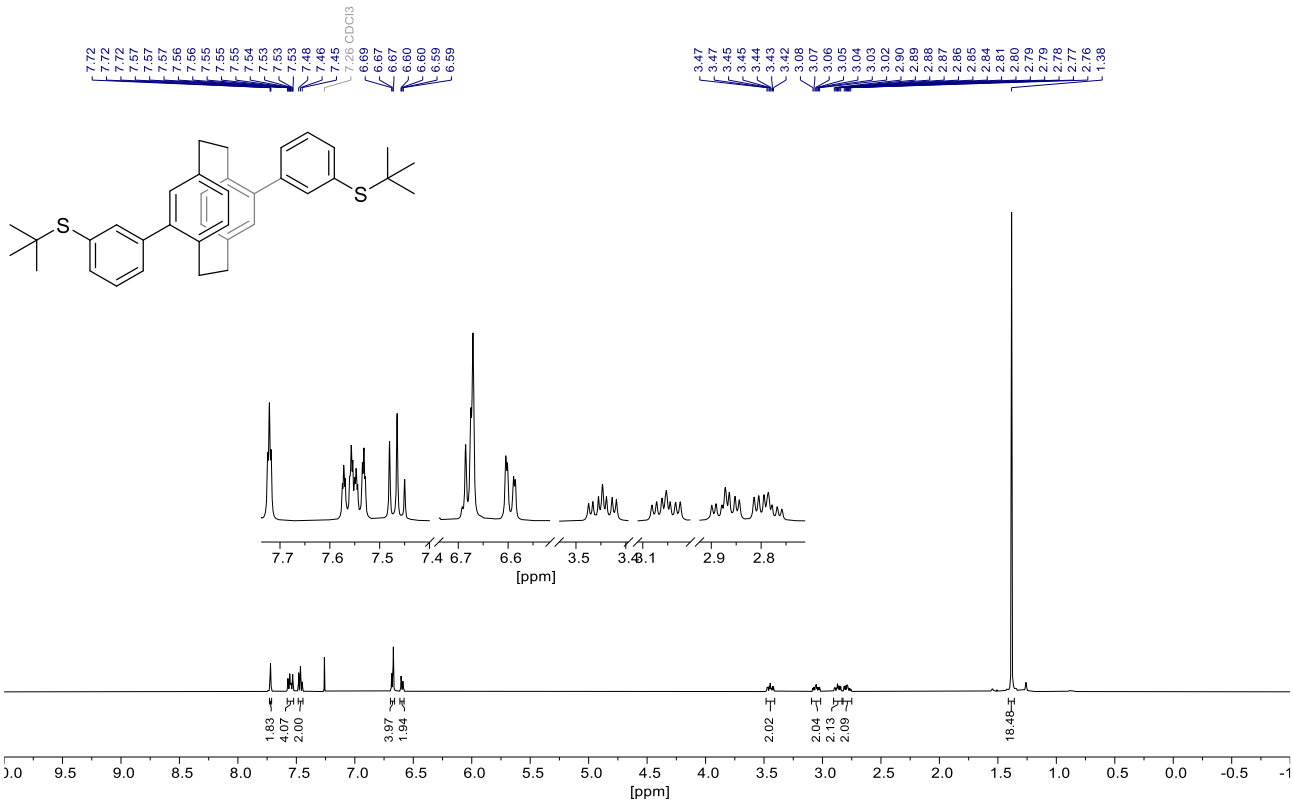

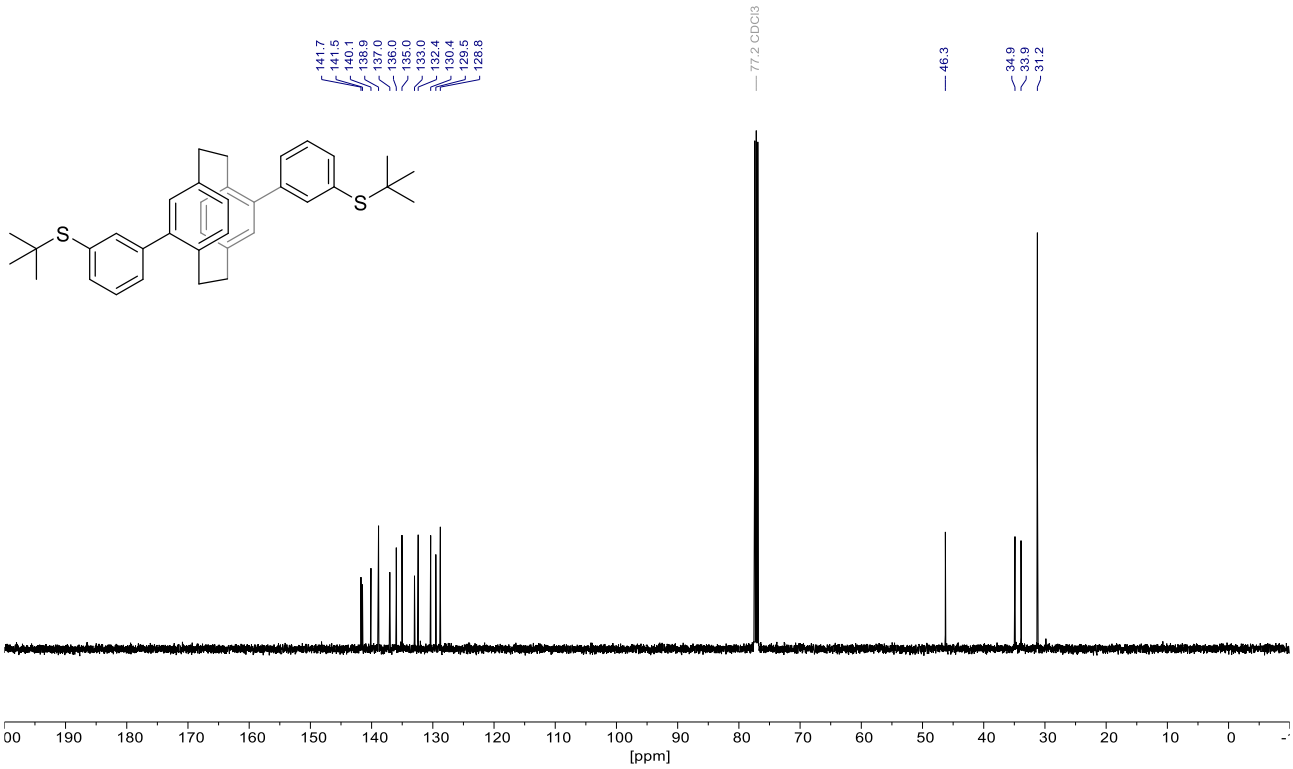

High Resolution Mass Spectrometry Report

Sample Name	**KR-168**	Instrument	maXis 4G
Comment	in MeOH+ AgNO3 (1mM)	Method	22 Direct_pos_mid.m

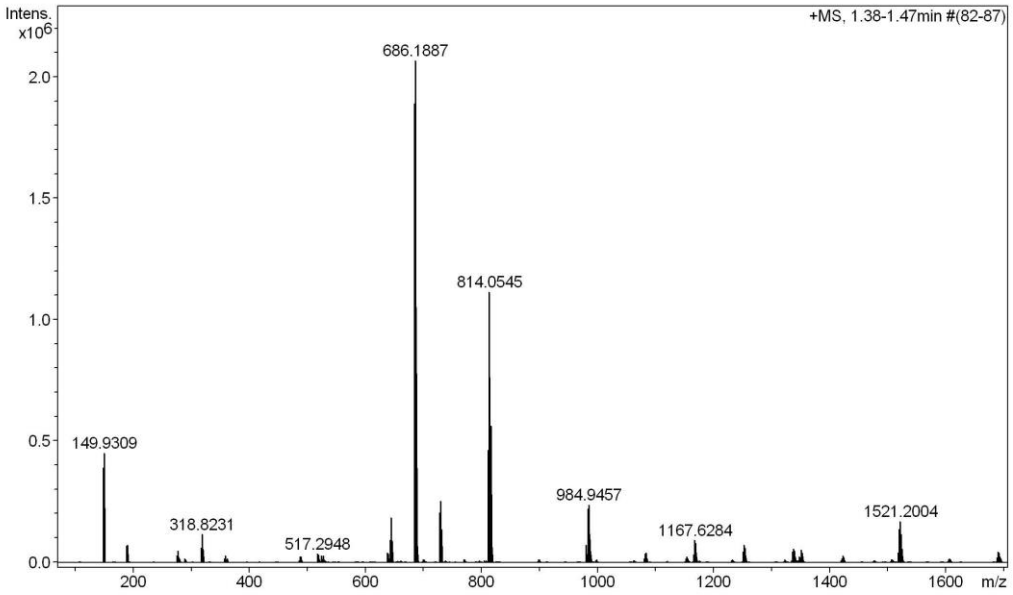

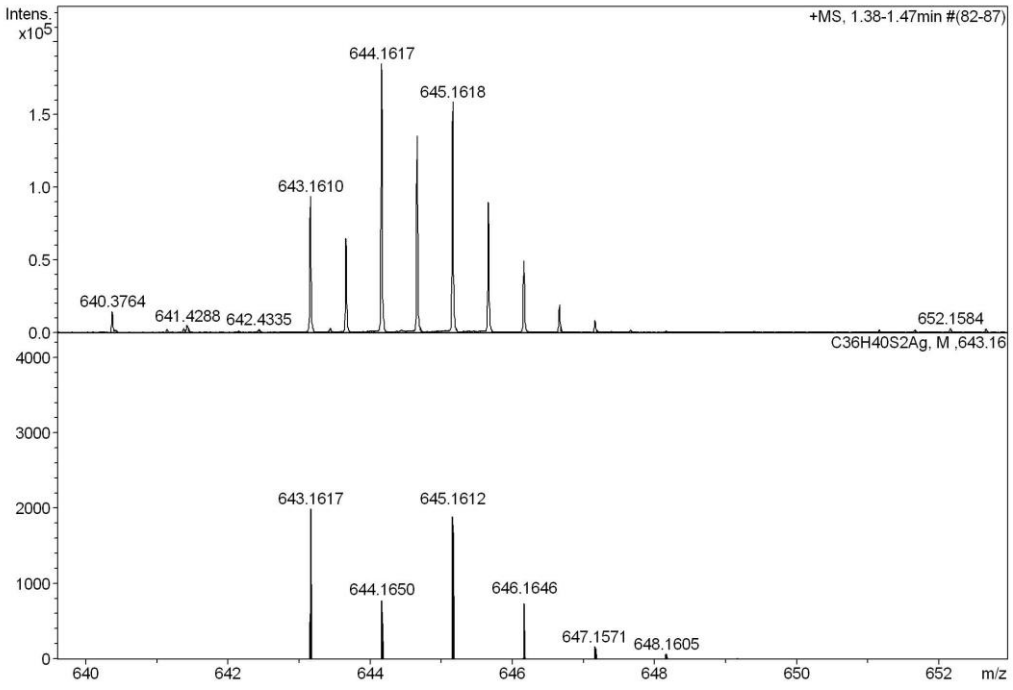

High Resolution Mass Spectrometry Report

Measured m/z vs. theoretical m/z

Meas. m/z	#	Formula	Score	m/z	err [mDa]	err [ppm]	mSigma	rdb	e⁻ Conf	z
643.1610	1	C 36 H 40 Ag S 2	100.00	643.1617	0.7	1.1	293.0	16.5	even	1+

Mass list

#	m/z	I %	I
1	147.9312	18.8	389268
2	149.9309	21.8	451621
3	188.9573	3.4	70271
4	190.9569	3.5	71482
5	275.7966	1.3	26828
6	277.7963	2.4	49709
7	316.8233	2.9	59523
8	318.8231	5.7	116904
9	320.8227	2.5	51865
10	359.8496	1.5	30367
11	517.2948	1.7	35064
12	519.2946	1.6	33150
13	525.2118	1.4	28896
14	527.2118	1.4	28663
15	637.3733	1.9	39343
16	639.3734	1.8	37374
17	643.1610	4.6	94388
18	643.6626	3.2	65222
19	644.1617	9.0	185578
20	644.6627	6.6	135848
21	645.1618	7.7	159043
22	645.6625	4.4	90336
23	646.1620	2.4	49784
24	684.1887	91.4	1890306
25	685.1914	34.9	722384
26	686.1887	100.0	2068073
27	687.1910	37.8	781310
28	688.1890	11.2	232171
29	689.1885	3.3	68240
30	727.6072	3.0	61701
31	728.1089	2.4	50471
32	728.6080	9.9	204185
33	729.1092	7.4	152583
34	729.6083	12.2	252757
35	730.1091	8.4	174099
36	730.6083	6.7	137821
37	731.1089	3.7	77529
38	731.6082	1.9	38610
39	812.0542	22.5	464648
40	813.0566	10.1	208728
41	814.0545	54.0	1116478
42	814.5542	1.7	34172
43	815.0568	20.1	415004
44	815.5545	1.3	27161
45	816.0541	27.3	565402
46	817.0560	9.3	192527
47	818.0539	3.1	64765
48	980.9454	3.5	73172
49	981.9480	1.6	32870
50	982.9458	10.7	220944
51	983.9483	4.3	88879
52	984.9457	11.6	239374
53	985.9479	4.3	89671
54	986.9453	4.6	95619
55	987.9474	1.6	33557
56	1082.1818	1.8	37301
57	1082.6822	1.7	35271
58	1083.1822	1.9	39448
59	1083.6824	1.6	32867
60	1165.6273	1.4	28661
61	1166.1287	1.5	31878
62	1166.6280	3.3	68509

#	m/z	I %	I
63	1167.1289	3.4	71073
64	1167.6284	4.5	92192
65	1168.1291	4.0	81940
66	1168.6287	3.7	75907
67	1169.1287	2.7	55121
68	1169.6286	1.9	38691
69	1251.0740	2.1	43450
70	1251.5746	2.1	44035
71	1252.0743	3.5	72679
72	1252.5750	3.3	67484
73	1253.0750	3.5	73035
74	1253.5752	2.9	60775
75	1254.0745	2.4	49800
76	1254.5745	1.7	34763
77	1336.5209	2.2	44598
78	1337.0211	2.1	43377
79	1337.5204	2.8	57168
80	1338.0212	2.3	48449
81	1338.5205	2.3	47646
82	1339.0212	1.7	36012
83	1339.5213	1.4	28790
84	1350.3075	2.6	53334
85	1351.3095	2.0	42288
86	1352.3077	2.1	42464
87	1353.3093	1.3	27181
88	1421.9673	1.3	26904
89	1517.1988	2.0	41485
90	1518.2023	1.7	35710
91	1519.1994	6.6	136915
92	1520.2019	5.3	108861
93	1521.2004	8.2	169619
94	1522.2019	5.7	118640
95	1523.2006	4.8	99479
96	1524.2012	2.7	56865
97	1525.2011	1.3	27609
98	1690.0927	2.2	46019
99	1691.0952	1.9	38978
100	1692.0936	2.0	41471

Acquisition Parameter

General	Fore Vacuum	2.48e+000 mBar	High Vacuum	1.14e-007 mBar	Source Type	ESI
	Scan Begin	75 m/z	Scan End	1700 m/z	Ion Polarity	Positive
Source	Set Nebulizer	0.4 Bar	Set Capillary	3600 V	Set Dry Gas	4.0 l/min
	Set Dry Heater	180 °C	Set End Plate Offset	-500 V		
Quadrupole	Set Ion Energy (MS only)	4.0 eV				
Coll. Cell	Collision Energy	8.0 eV	Set Collision Cell RF	350.0 Vpp	100.0 Vpp	
Ion Cooler	Set Ion Cooler Transfer Time	75.0 µs	Set Ion Cooler Pre Pulse Storage Time	10.0 µs		

^{1}H, ^{13}C{^{1}H} NMR ($CDCl_3$, 500/126 MHz) and HR-MS spectra of ps-*para-meta* PCP (3a)

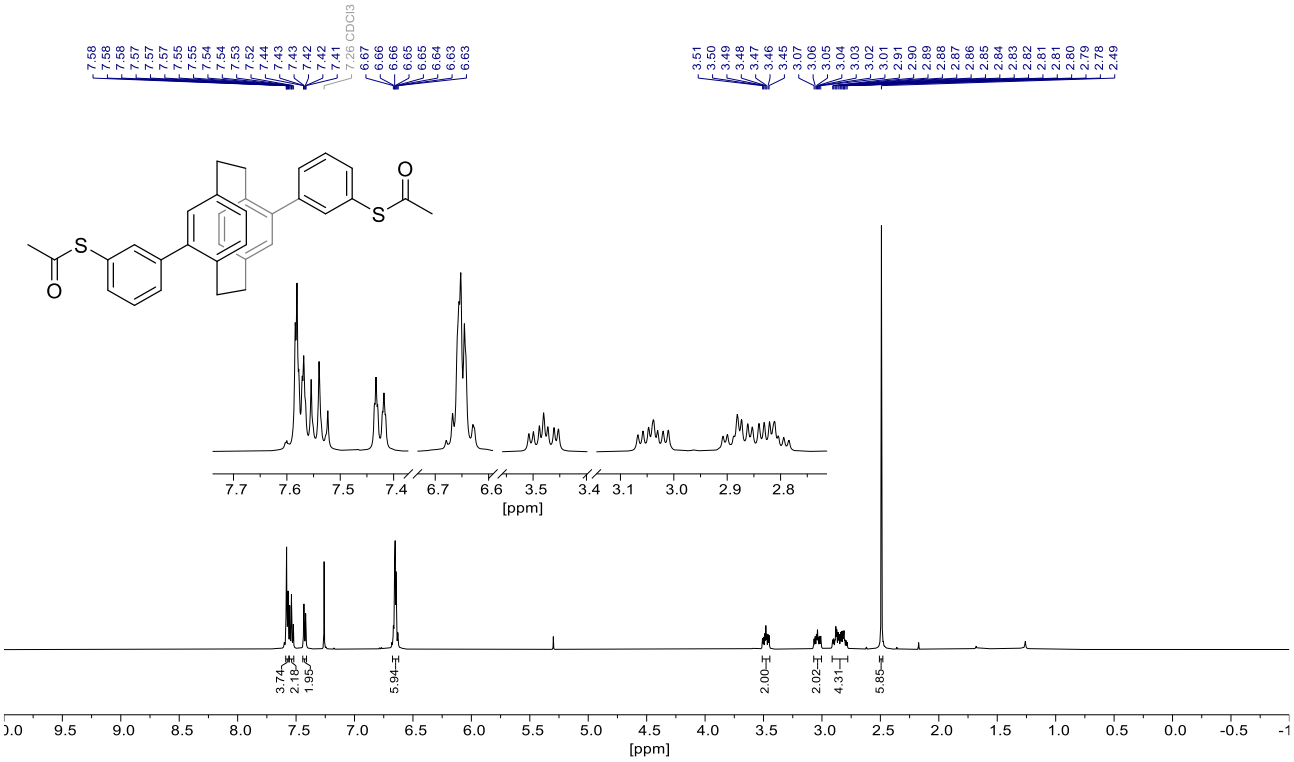

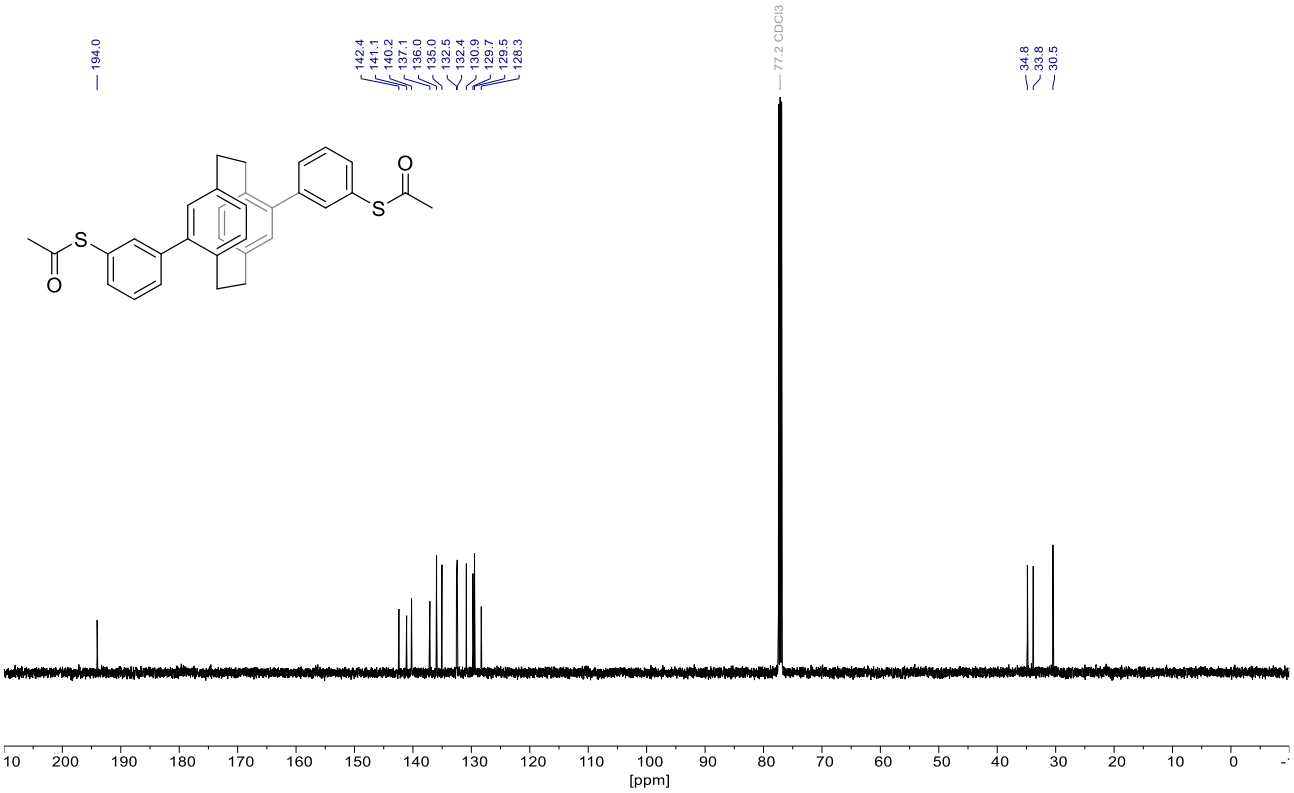

High Resolution Mass Spectrometry Report

Sample Name	**Ksenia Reznikova / KR 178**	Instrument	maXis 4G
Comment	10 ug / mL in DCM, analyzed in MeOH+AgNO3 5mM	Method	23 Direct_pos_higher.m

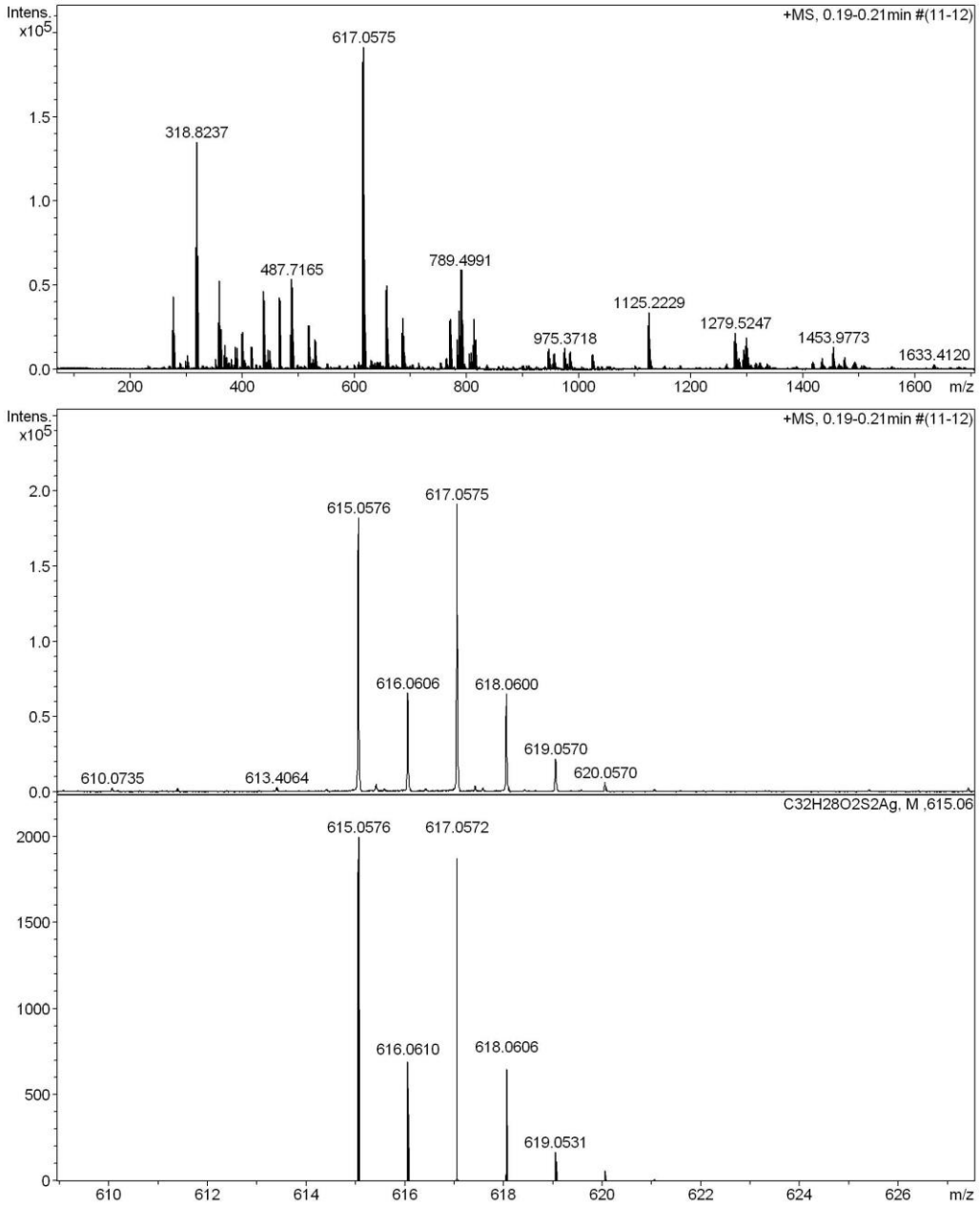

High Resolution Mass Spectrometry Report

Measured m/z vs. theoretical m/z

Meas. m/z	#	Formula	Score	m/z	err [mDa]	err [ppm]	mSigma	rdb	e⁻ Conf	z
615.0576	1	C 32 H 28 Ag O 2 S 2	100.00	615.0576	0.0	0.1	16.1	18.5	even	1+

Mass list

#	m/z	I %	I
1	275.7970	12.3	23666
2	277.7967	22.7	43541
3	279.7964	10.9	20989
4	301.8333	4.7	8952
5	316.8238	38.0	72843
6	318.8237	70.5	135252
7	320.8232	35.5	67977
8	357.8505	14.6	28038
9	359.8501	27.5	52648
10	361.8498	12.7	24275
11	367.8210	4.5	8543
12	369.8206	7.7	14737
13	388.1757	7.2	13887
14	390.1755	6.9	13274
15	399.1079	11.2	21421
16	401.1078	11.6	22306
17	415.1025	7.1	13581
18	417.1030	7.1	13648
19	437.1813	24.4	46812
20	438.1845	5.5	10560
21	439.1810	21.5	41285
22	440.1843	4.8	9149
23	446.6898	6.4	12260
24	448.6894	6.1	11629
25	465.2125	22.4	42981
26	466.2157	5.2	9877
27	467.2123	21.6	41457
28	468.2157	5.2	9938
29	485.7166	10.9	20803
30	487.7165	28.1	53844
31	489.7163	25.6	49023
32	491.7158	8.8	16811
33	517.2954	13.7	26180
34	518.2987	5.0	9673
35	519.2950	13.8	26420
36	528.7429	9.3	17923
37	530.7430	8.9	17110
38	615.0576	95.3	182661
39	616.0606	34.5	66068
40	617.0575	100.0	191719
41	618.0600	34.1	65355
42	619.0570	11.8	22541
43	656.0838	24.7	47436
44	657.0868	10.1	19450
45	658.0836	26.2	50185
46	659.0866	9.8	18720
47	684.1877	11.5	21983
48	685.1907	4.7	8991
49	686.1880	16.1	30859
50	687.1912	6.5	12434
51	688.1886	10.5	20116
52	690.1886	4.5	8541
53	769.3519	15.1	28960
54	770.3546	7.4	14242
55	771.3518	15.7	30076
56	772.3543	6.8	12965
57	783.9514	9.3	17846
58	785.9511	18.3	35043
59	786.9539	7.0	13439
60	787.9507	10.5	20142
61	789.4991	31.0	59366
62	790.5021	14.3	27368

#	m/z	I %	I
63	791.4993	31.0	59338
64	792.5019	14.3	27416
65	793.5031	4.8	9112
66	805.4939	5.1	9735
67	807.4933	5.3	10187
68	812.0556	7.7	14702
69	814.0559	15.8	30282
70	815.0584	6.4	12320
71	816.0558	9.3	17892
72	945.3382	5.8	11083
73	947.3400	6.7	12824
74	954.8482	4.9	9299
75	956.8479	5.0	9552
76	973.3714	5.4	10322
77	975.3718	6.7	12895
78	982.9529	5.1	9782
79	984.9532	5.7	10870
80	1023.5182	4.5	8544
81	1025.5196	4.8	9255
82	1123.2227	13.6	26119
83	1124.2248	10.5	20112
84	1125.2229	17.8	34134
85	1126.2255	11.7	22372
86	1127.2249	6.5	12370
87	1277.5239	8.8	16794
88	1278.5268	7.7	14792
89	1279.5247	11.6	22234
90	1280.5284	8.3	15920
91	1294.1245	6.2	11821
92	1296.1262	4.9	9423
93	1297.6717	7.4	14116
94	1298.6742	5.9	11274
95	1299.6735	10.1	19295
96	1300.6760	6.8	13109
97	1451.9765	5.2	9917
98	1452.9797	4.7	8968
99	1453.9773	7.0	13482
100	1454.9801	5.5	10472

Acquisition Parameter

General	Fore Vacuum	2.59e+000 mBar	High Vacuum	9.65e-008 mBar	Source Type	ESI
	Scan Begin	75 m/z	Scan End	1700 m/z	Ion Polarity	Positive
Source	Set Nebulizer	0.4 Bar	Set Capillary	3600 V	Set Dry Gas	4.0 l/min
	Set Dry Heater	180 °C	Set End Plate Offset	-500 V		
Quadrupole	Set Ion Energy (MS only)	4.0 eV				
Coll. Cell	Collision Energy	8.0 eV	Set Collision Cell RF	500.0 Vpp		
Ion Cooler	Set Ion Cooler Transfer Time	100.0 µs	Set Ion Cooler Pre Pulse Storage Time	18.0 µs		

^{1}H, ^{13}C{^{1}H} NMR ($CDCl_3$, 500/126 MHz) and HR-MS spectra of ps-*meta-para* S*t*Bu PCP (11)

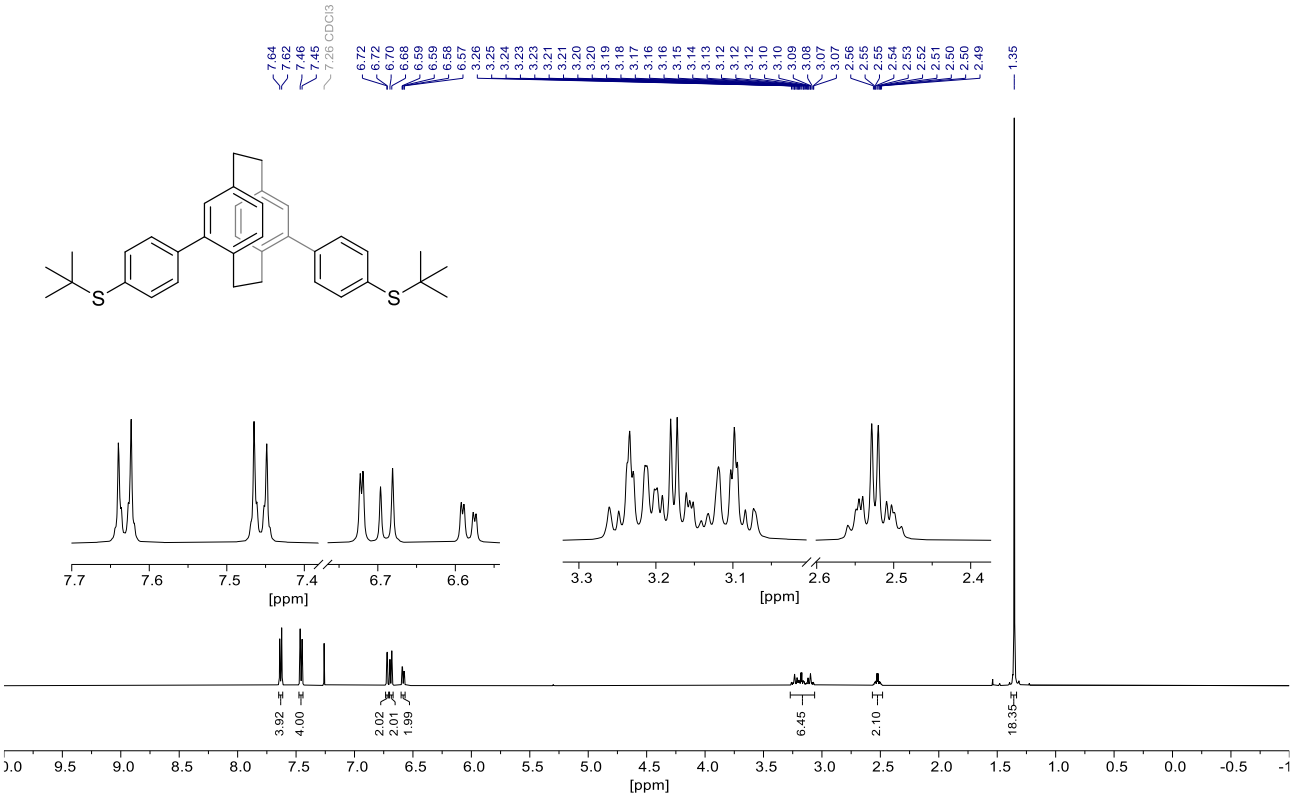

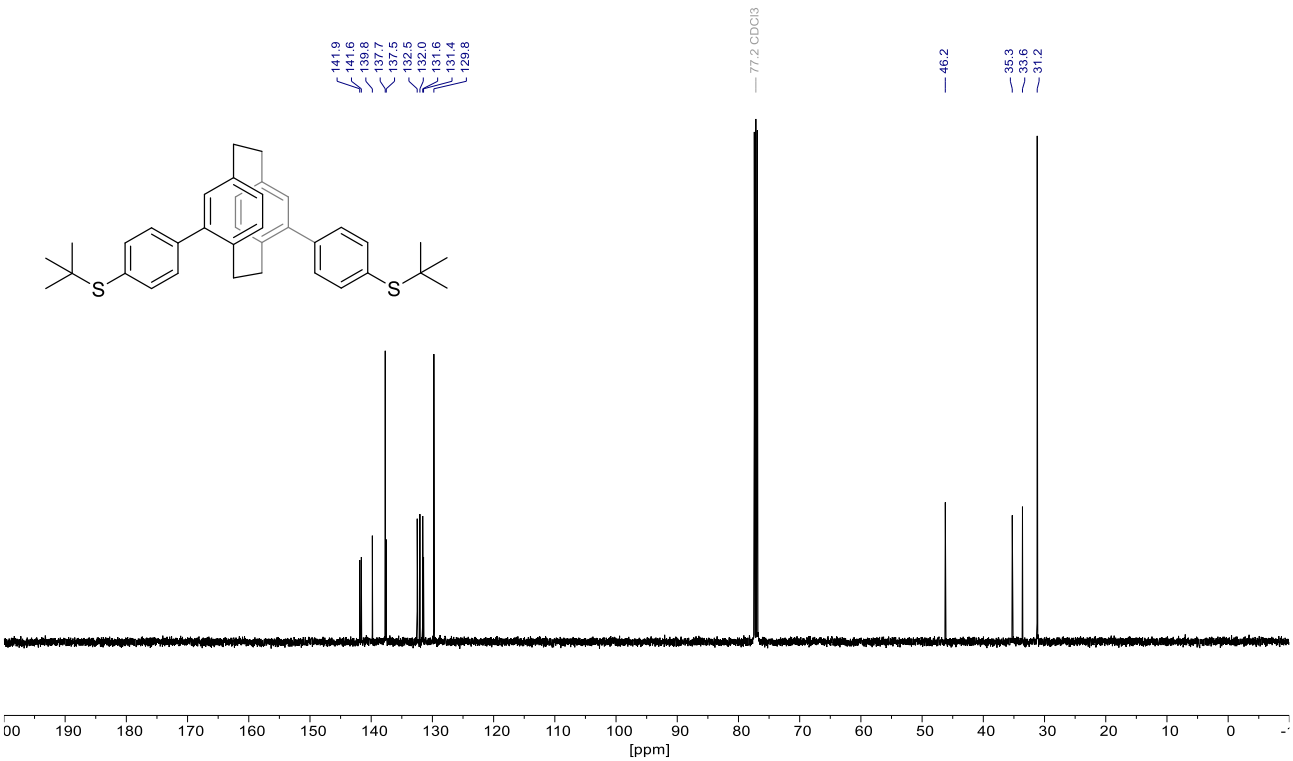

High Resolution Mass Spectrometry Report

Sample Name	**Ksenia Reznikova / KR 166**	Instrument	maXis 4G
Comment	10 ug / mL in DCM, analyzed in MeOH+AgNO3 5mM	Method	23 Direct_pos_higher.m

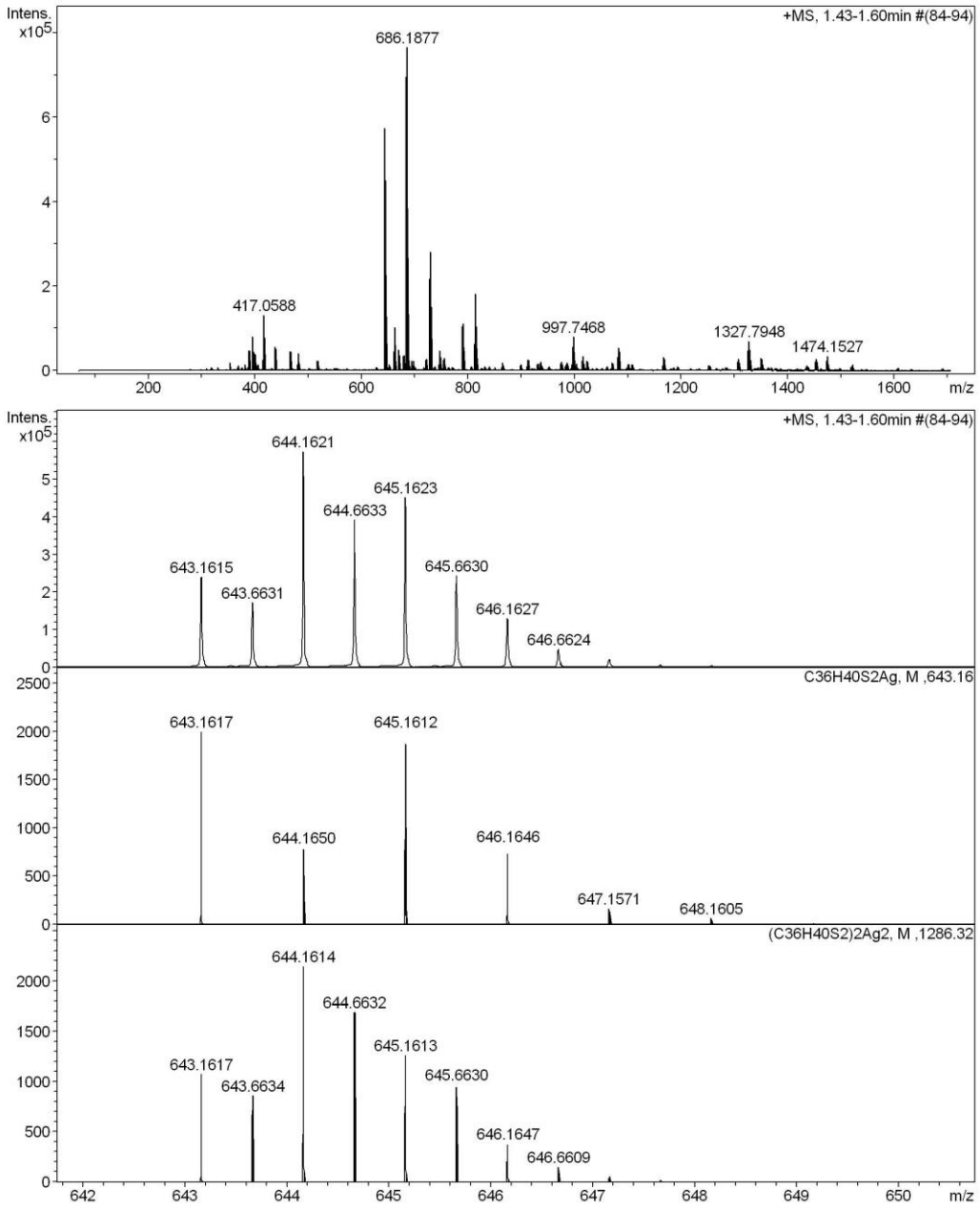

High Resolution Mass Spectrometry Report

Measured m/z vs. theoretical m/z

Meas. m/z	#	Formula	Score	m/z	err [mDa]	err [ppm]	mSigma	rdb	e^- Conf	z
643.1615	1	C 36 H 40 Ag S 2	100.00	643.1617	0.2	0.3	320.0	16.5	even	1+

Mass list

#	m/z	I %	I
1	388.1743	6.2	47551
2	390.1744	6.1	46954
3	395.5449	5.3	40379
4	396.5450	10.6	81329
5	397.0463	4.7	35899
6	397.5448	6.1	46752
7	399.1068	5.3	40724
8	401.1067	5.1	38760
9	416.0588	8.8	67005
10	416.5603	4.1	31707
11	417.0588	17.3	132215
12	417.5602	7.9	60584
13	418.0588	10.2	77837
14	418.5599	4.4	33699
15	437.1806	7.5	57425
16	439.1804	6.9	52638
17	465.2119	6.1	46456
18	467.2120	5.9	44976
19	480.9924	5.0	38205
20	481.9923	5.3	40557
21	643.1615	31.5	241523
22	643.6631	22.5	172602
23	644.1621	75.0	574700
24	644.6633	51.3	393098
25	645.1623	59.1	452473
26	645.6630	32.0	245069
27	646.1627	17.0	130443
28	646.6624	6.4	49310
29	661.1481	6.1	46837
30	661.6493	4.9	37844
31	662.1483	13.3	102037
32	662.6494	9.8	74769
33	663.1486	10.0	76413
34	663.6493	6.4	48658
35	670.1454	6.5	49687
36	670.6465	4.9	37150
37	671.1456	4.9	37375
38	679.1340	4.6	35133
39	681.1340	5.0	38066
40	684.1878	90.9	696002
41	685.1908	33.8	258945
42	686.1877	100.0	765771
43	687.1902	35.0	268172
44	688.1883	11.5	87696
45	722.1605	3.7	28313
46	727.6081	8.5	65380
47	728.1098	7.4	56802
48	728.6086	28.5	218196
49	729.1100	21.4	164250
50	729.6090	36.8	281790
51	730.1099	24.8	189765
52	730.6091	19.8	151516
53	731.1095	11.1	85163
54	731.6091	5.6	42881
55	746.5950	5.2	40065
56	747.0964	4.2	32029
57	747.5954	6.2	47777
58	748.0962	4.4	33584
59	748.5955	3.6	27335
60	755.1013	3.8	29471
61	755.5968	3.9	30188
62	789.4979	13.8	105944

High Resolution Mass Spectrometry Report

#	m/z	I %	I
63	790.5011	6.3	48168
64	791.4984	14.6	111681
65	792.5008	6.2	47337
66	812.0555	8.3	63347
67	813.0570	8.6	65615
68	813.5575	4.6	35135
69	814.0561	24.0	183512
70	814.5574	7.1	54609
71	815.0575	13.9	106166
72	815.5572	5.6	42509
73	816.0559	11.5	87919
74	817.0572	4.0	30375
75	996.7461	6.9	52893
76	997.2474	7.4	56659
77	997.7468	10.6	81004
78	998.2476	9.2	70069
79	998.7474	7.9	60636
80	999.2476	5.6	42799
81	1015.7345	4.6	35450
82	1016.2350	4.1	31313
83	1081.1986	3.6	27249
84	1081.7001	4.1	31706
85	1082.1988	6.8	52334
86	1082.7001	6.7	51416
87	1083.1995	7.3	55656
88	1083.7001	6.1	46619
89	1084.1997	4.5	34534
90	1167.6527	4.2	32220
91	1168.1536	3.7	27996
92	1307.6452	3.7	28642
93	1325.7937	6.3	48324
94	1326.7968	5.6	43181
95	1327.7948	9.3	70911
96	1328.7971	6.6	50597
97	1350.3554	3.8	29426
98	1351.3569	3.8	28985
99	1454.0035	3.7	28562
100	1474.1527	4.6	35176

Acquisition Parameter

General	Fore Vacuum	2.59e+000 mBar	High Vacuum	9.68e-008 mBar	Source Type	ESI
	Scan Begin	75 m/z	Scan End	1700 m/z	Ion Polarity	Positive
Source	Set Nebulizer	0.4 Bar	Set Capillary	3600 V	Set Dry Gas	4.0 l/min
	Set Dry Heater	180 °C	Set End Plate Offset	-500 V		
Quadrupole	Set Ion Energy (MS only)	4.0 eV				
Coll. Cell	Collision Energy	8.0 eV	Set Collision Cell RF	500.0 Vpp		
Ion Cooler	Set Ion Cooler Transfer Time	100.0 µs	Set Ion Cooler Pre Pulse Storage Time	18.0 µs		

^{1}H, $^{13}C\{^{1}H\}$ NMR ($CDCl_3$, 500/126 MHz) and HR-MS spectra of ps-*meta-para* PCP (2a)

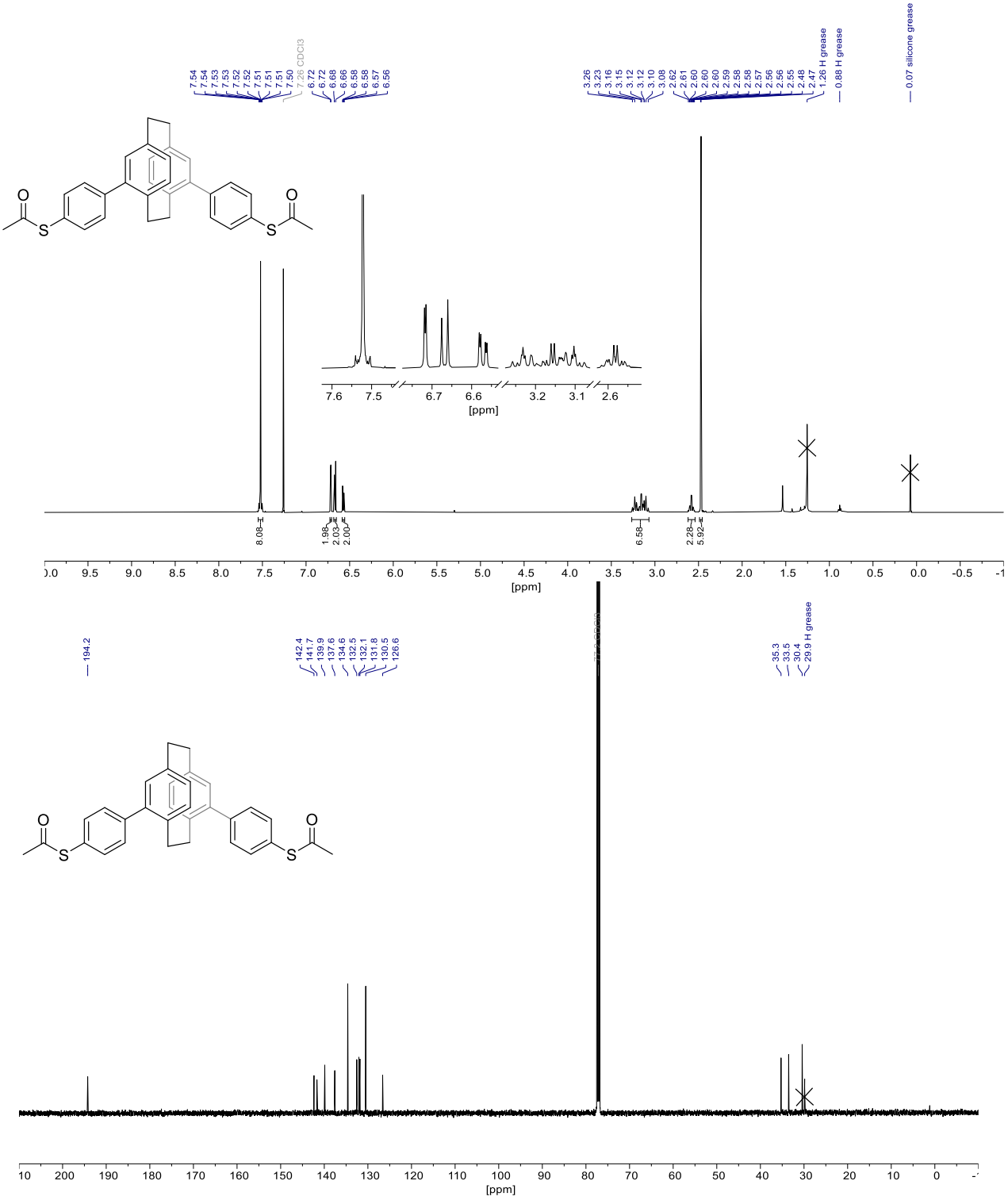

High Resolution Mass Spectrometry Report

Sample Name	**Ksenia Reznikova / KR 212**	Instrument	maXis 4G
Comment	10 ug / mL in DCM, analyzed in MeOH+AgNO3 5mM	Method	23 Direct_pos_higher.m

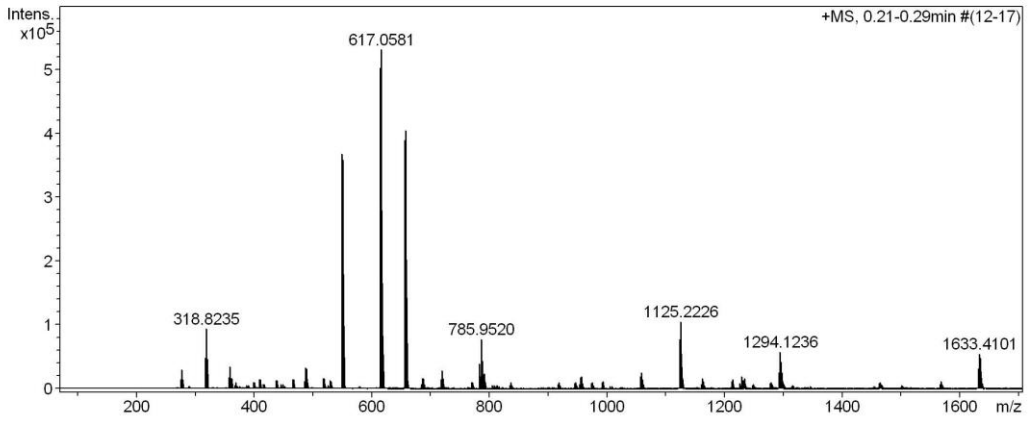

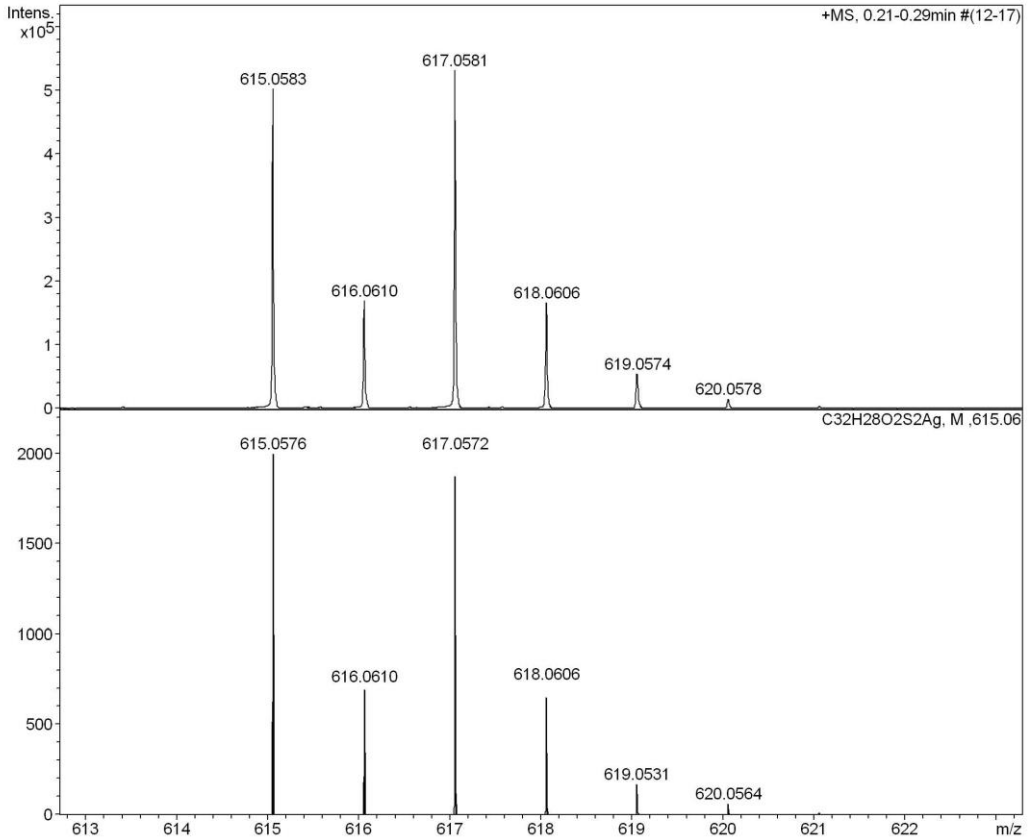

High Resolution Mass Spectrometry Report

Measured m/z vs. theoretical m/z

Meas. m/z	#	Formula	Score	m/z	err [mDa]	err [ppm]	mSigma	rdb	e¯ Conf	z
615.0583	1	C 32 H 28 Ag O 2 S 2	100.00	615.0576	-0.7	-1.1	21.8	18.5	even	1+

Mass list

#	m/z	I %	I
1	275.7969	2.9	15572
2	277.7966	5.6	29917
3	279.7962	2.7	14576
4	316.8237	9.2	48685
5	318.8235	17.7	94297
6	320.8231	8.7	46407
7	357.8504	3.5	18653
8	359.8501	6.6	35050
9	361.8498	3.2	17014
10	369.8208	2.0	10659
11	399.1080	2.1	10943
12	401.1078	2.1	11011
13	408.9479	2.9	15206
14	410.9469	2.8	14946
15	437.1811	2.6	13830
16	439.1810	2.4	12853
17	465.2123	2.9	15522
18	467.2123	2.8	14650
19	485.7170	2.4	12578
20	487.7167	6.4	33854
21	489.7162	6.0	31872
22	491.7158	2.0	10727
23	517.2955	3.2	17090
24	519.2953	3.0	15974
25	528.7431	2.4	12655
26	530.7431	2.3	11977
27	549.1231	69.1	367566
28	550.1258	19.0	100959
29	551.1229	67.6	359303
30	552.1254	18.7	99249
31	553.1240	4.7	25228
32	615.0583	94.5	502324
33	616.0610	31.9	169795
34	617.0581	100.0	531631
35	618.0606	31.4	166745
36	619.0574	10.3	54831
37	620.0578	3.0	15970
38	656.0848	73.4	390175
39	657.0875	25.5	135747
40	658.0846	76.0	404282
41	659.0871	26.9	143168
42	660.0843	9.3	49519
43	661.0846	2.6	13816
44	686.1882	3.0	16134
45	688.1886	3.0	15711
46	718.0153	2.9	15285
47	720.0153	5.4	28801
48	722.0154	3.1	16334
49	769.3515	2.0	10369
50	783.9518	7.4	39281
51	784.9548	2.8	15080
52	785.9520	14.7	78353
53	786.9543	5.5	29277
54	787.9513	8.3	44202
55	788.9538	3.0	15797
56	789.4987	4.1	21936
57	790.5015	2.1	10989
58	791.4990	4.6	24343
59	792.5020	2.1	10963
60	836.9494	1.9	10349
61	954.8485	3.5	18500
62	956.8483	3.6	19338

High Resolution Mass Spectrometry Report

#	m/z	I %	I
63	993.3463	2.1	11403
64	1057.2832	3.7	19418
65	1058.2867	2.5	13131
66	1059.2844	4.8	25461
67	1060.2867	2.8	14742
68	1123.2219	14.6	77491
69	1124.2250	10.9	57889
70	1125.2226	19.8	105219
71	1126.2249	12.5	66588
72	1127.2239	6.6	34831
73	1128.2242	3.0	15696
74	1162.2461	3.2	17017
75	1164.2462	2.2	11530
76	1211.5842	2.1	11396
77	1213.5855	2.7	14210
78	1228.1846	3.7	19687
79	1229.1874	2.2	11647
80	1230.1847	2.6	13826
81	1231.7312	2.6	13719
82	1232.7343	2.0	10898
83	1233.7322	3.2	17227
84	1234.7355	2.2	11817
85	1279.5236	2.0	10381
86	1292.1233	4.8	25440
87	1293.1259	3.6	19259
88	1294.1236	10.9	57960
89	1295.1266	7.6	40302
90	1296.1241	8.1	43236
91	1297.1257	5.0	26326
92	1298.1258	2.5	13353
93	1567.4685	2.2	11848
94	1568.4704	2.0	10397
95	1631.4078	6.0	32062
96	1632.4114	6.6	34919
97	1633.4101	10.4	55447
98	1634.4121	9.1	48363
99	1635.4116	6.0	31975
100	1636.4123	3.4	18131

Acquisition Parameter

General	Fore Vacuum	2.59e+000 mBar	High Vacuum	9.65e-008 mBar	Source Type	ESI
	Scan Begin	75 m/z	Scan End	1700 m/z	Ion Polarity	Positive
Source	Set Nebulizer	0.4 Bar	Set Capillary	3600 V	Set Dry Gas	4.0 l/min
	Set Dry Heater	180 °C	Set End Plate Offset	-500 V		
Quadrupole	Set Ion Energy (MS only)	4.0 eV				
Coll. Cell	Collision Energy	8.0 eV	Set Collision Cell RF	500.0 Vpp		
Ion Cooler	Set Ion Cooler Transfer Time	100.0 µs	Set Ion Cooler Pre Pulse Storage Time	18.0 µs		

^{1}H, ^{13}C{^{1}H} NMR ($CDCl_3$, 500/126 MHz) and HR-MS spectra of ps-*meta-meta* S*t*Bu PCP (12)

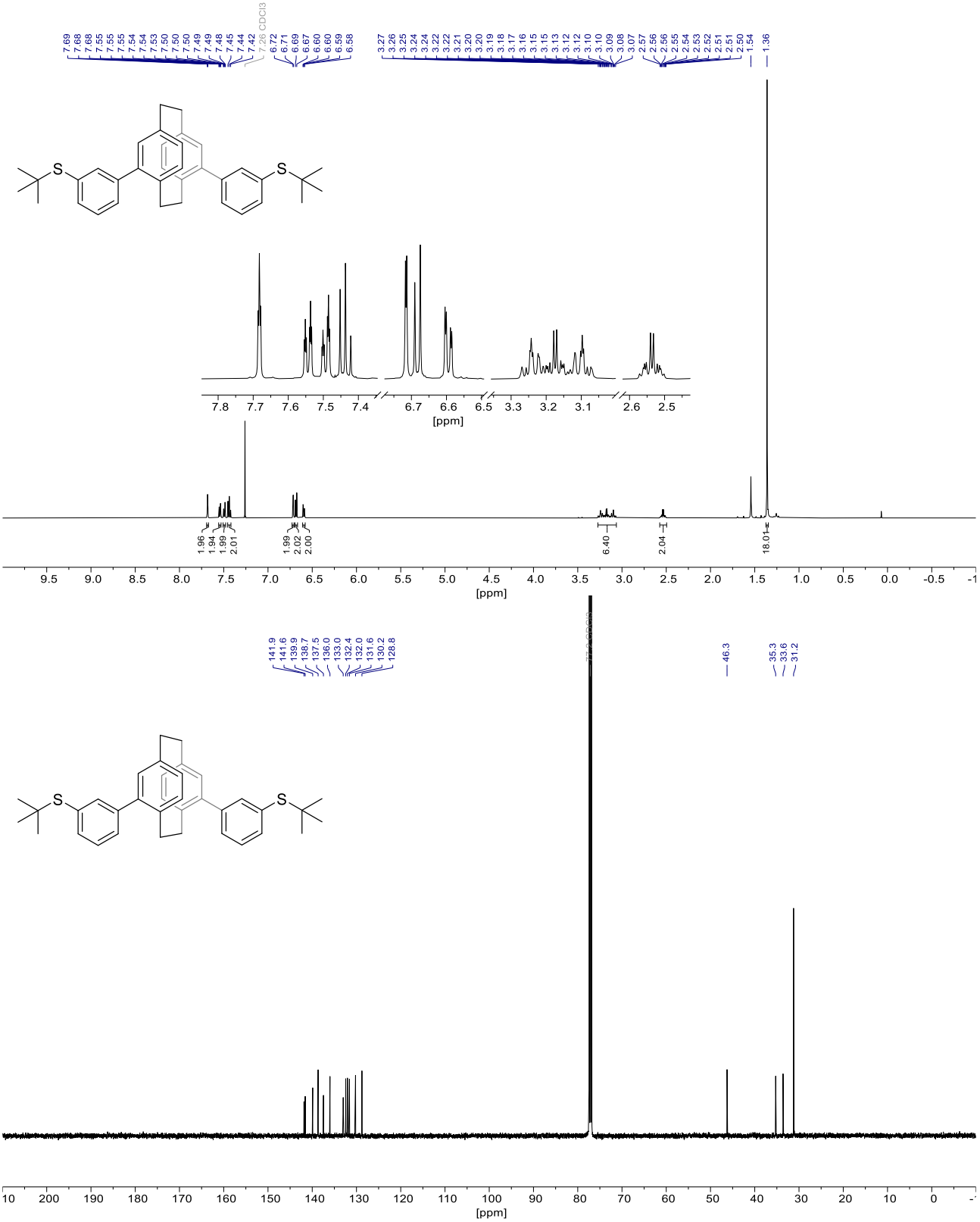

High Resolution Mass Spectrometry Report

Sample Name	**Ksenia Reznikova / KR 167**	Instrument	maXis 4G
Comment	10 ug / mL in DCM, analyzed in MeOH+AgNO3 5mM	Method	23 Direct_pos_higher.m

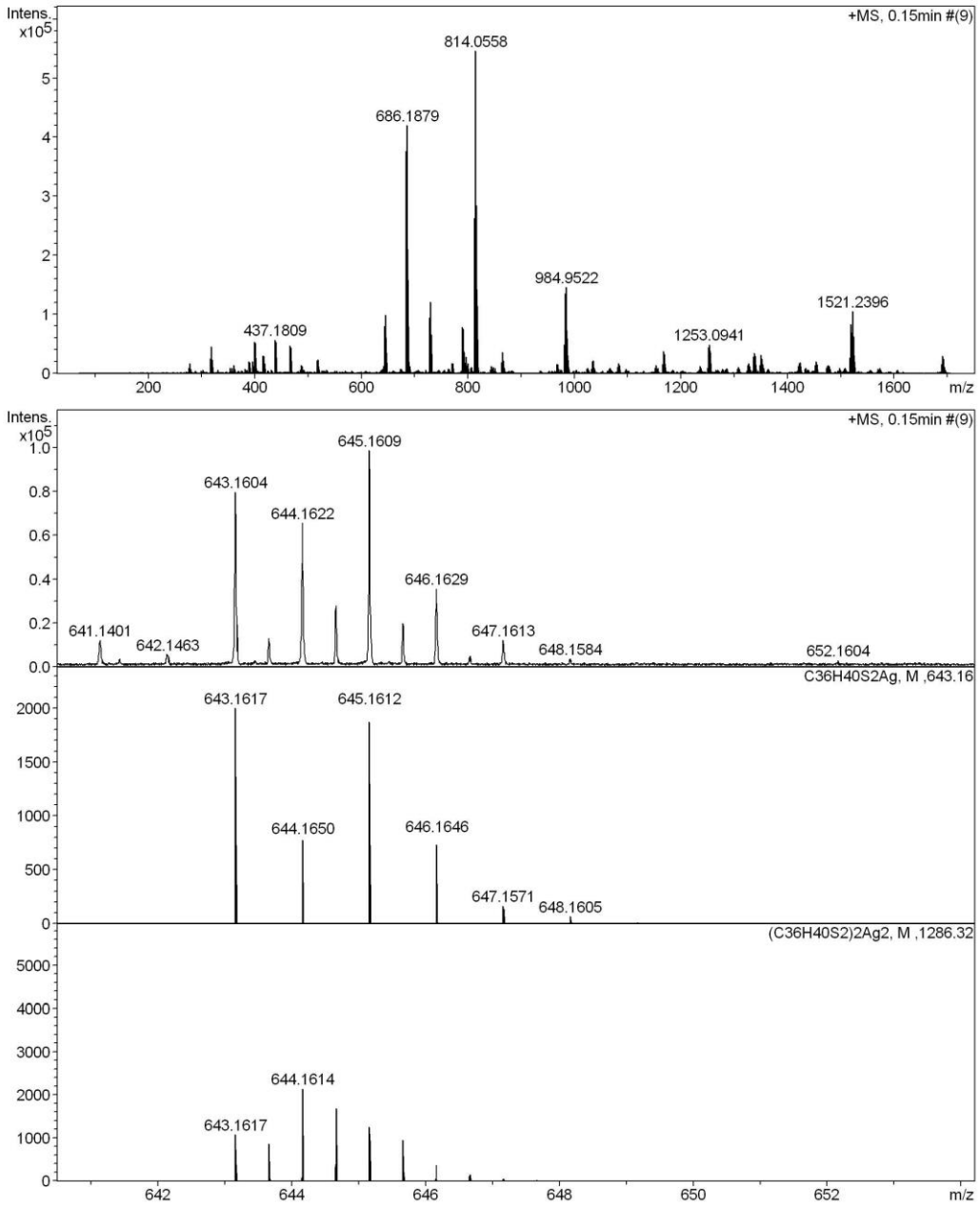

High Resolution Mass Spectrometry Report

Measured m/z vs. theoretical m/z

Meas. m/z	#	Formula	Score	m/z	err [mDa]	err [ppm]	mSigma	rdb	e⁻ Conf	z
643.1604	1	C 36 H 40 Ag S 2	100.00	643.1617	1.3	2.0	117.6	16.5	even	1+

Mass list

#	m/z	I %	I
1	316.8236	4.6	24986
2	318.8234	8.3	45604
3	320.8227	4.3	23530
4	388.1756	3.9	21376
5	390.1753	3.6	19860
6	396.5457	3.8	20814
7	399.1078	10.0	54398
8	401.1076	9.5	52178
9	415.1027	5.6	30846
10	417.0596	5.6	30334
11	417.1026	5.7	30925
12	437.1809	10.5	57229
13	439.1807	9.8	53698
14	465.2122	8.7	47604
15	467.2122	8.3	45137
16	517.2951	4.2	23177
17	519.2951	4.3	23572
18	643.1604	14.6	79965
19	644.1622	12.0	65718
20	644.6622	5.1	27922
21	645.1609	18.1	98801
22	645.6625	3.6	19877
23	646.1629	6.6	35912
24	684.1881	69.0	377318
25	685.1908	28.2	154362
26	686.1879	76.9	420044
27	687.1903	29.2	159770
28	688.1884	12.3	67288
29	689.1889	3.9	21402
30	727.6082	5.9	32090
31	728.1098	4.6	25168
32	728.6089	17.2	94229
33	729.1099	14.0	76597
34	729.6088	22.1	120896
35	730.1105	15.1	82433
36	730.6092	12.3	67078
37	731.1092	7.7	41925
38	731.6094	3.8	20790
39	789.4978	14.4	78770
40	790.5009	6.9	37825
41	791.4983	13.9	76074
42	792.5008	6.6	35842
43	797.0640	5.3	28820
44	812.0559	48.1	262717
45	813.0585	18.7	102440
46	814.0558	100.0	546516
47	815.0584	37.2	203105
48	816.0556	52.3	285774
49	817.0577	21.2	116037
50	818.0548	6.9	37945
51	863.0527	3.5	19289
52	865.0531	6.7	36889
53	867.0524	4.1	22672
54	980.9515	9.1	49798
55	981.9555	3.9	21308
56	982.9522	24.7	135017
57	983.9550	10.5	57282
58	984.9522	26.8	146340
59	985.9546	10.5	57646
60	986.9519	11.0	59988
61	987.9549	4.5	24765
62	1033.9503	4.0	21597

High Resolution Mass Spectrometry Report

#	m/z	I %	I
63	1035.9504	4.0	21808
64	1166.6426	5.4	29345
65	1167.1446	5.8	31622
66	1167.6432	7.0	38369
67	1168.1436	6.1	33314
68	1168.6431	6.2	33678
69	1169.1443	4.6	25312
70	1251.0944	5.4	29249
71	1251.5949	5.4	29270
72	1252.0945	8.1	44178
73	1252.5948	7.4	40386
74	1253.0941	9.1	49640
75	1253.5948	7.0	38241
76	1254.0950	6.6	35916
77	1254.5948	4.2	23118
78	1336.5457	5.3	29085
79	1337.0462	5.1	27864
80	1337.5466	6.4	35244
81	1338.0460	6.0	33061
82	1338.5467	5.5	29998
83	1339.0456	4.4	24125
84	1339.5456	3.6	19556
85	1350.3331	5.9	32257
86	1351.3357	4.7	25724
87	1352.3338	4.3	23570
88	1453.9729	3.8	20621
89	1517.2378	4.8	26472
90	1518.2414	4.2	22788
91	1519.2386	15.3	83590
92	1520.2410	12.7	69337
93	1521.2396	19.3	105338
94	1522.2412	13.7	74884
95	1523.2403	11.5	62782
96	1524.2408	6.5	35322
97	1525.2425	3.7	20461
98	1690.1485	5.6	30777
99	1691.1477	4.4	24241
100	1692.1488	4.7	25510

Acquisition Parameter

General	Fore Vacuum	2.59e+000 mBar	High Vacuum	9.68e-008 mBar	Source Type	ESI
	Scan Begin	75 m/z	Scan End	1700 m/z	Ion Polarity	Positive
Source	Set Nebulizer	0.4 Bar	Set Capillary	3600 V	Set Dry Gas	4.0 l/min
	Set Dry Heater	180 °C	Set End Plate Offset	-500 V		
Quadrupole	Set Ion Energy (MS only)	4.0 eV				
Coll. Cell	Collision Energy	8.0 eV	Set Collision Cell RF	500.0 Vpp		
Ion Cooler	Set Ion Cooler Transfer Time	100.0 µs	Set Ion Cooler Pre Pulse Storage Time	18.0 µs		

^{1}H, ^{13}C{^{1}H} NMR (CDCl3, 500/126 MHz) and HR-MS spectra of ps-*meta-meta* PCP (4a)

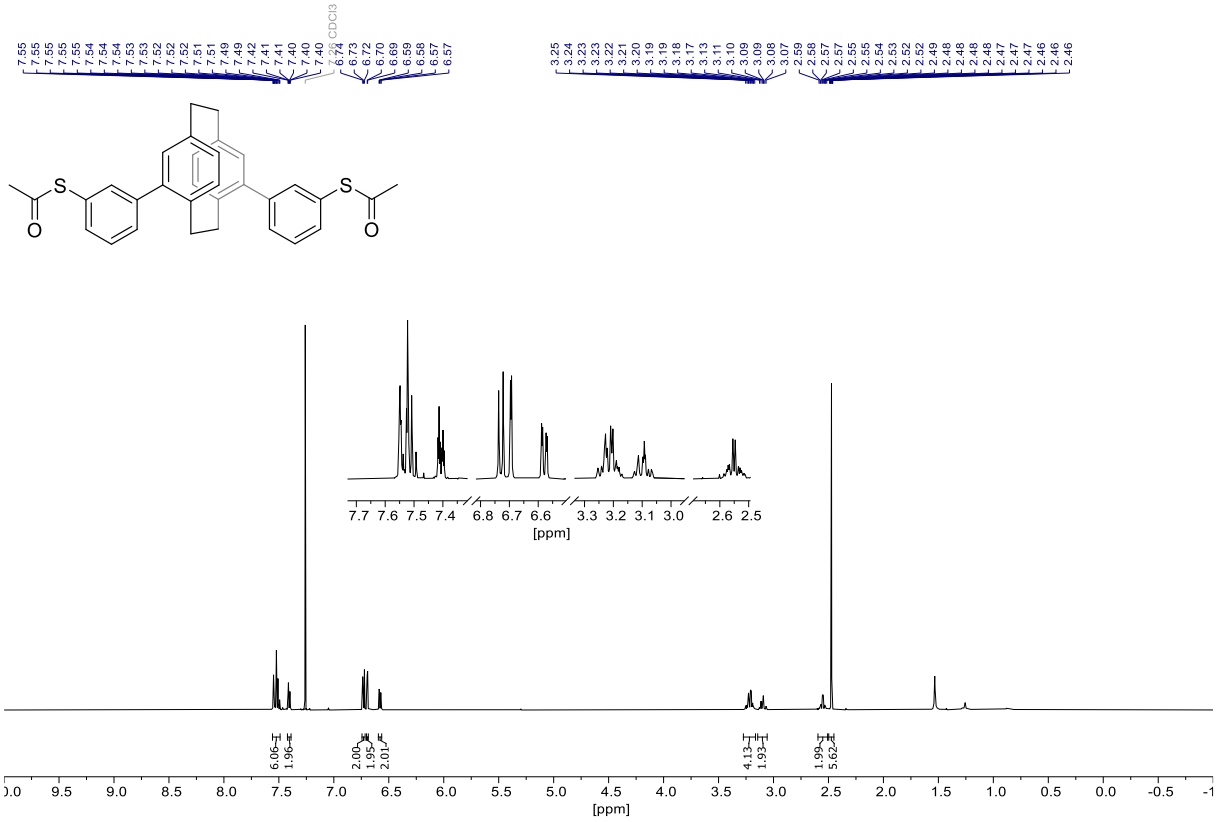

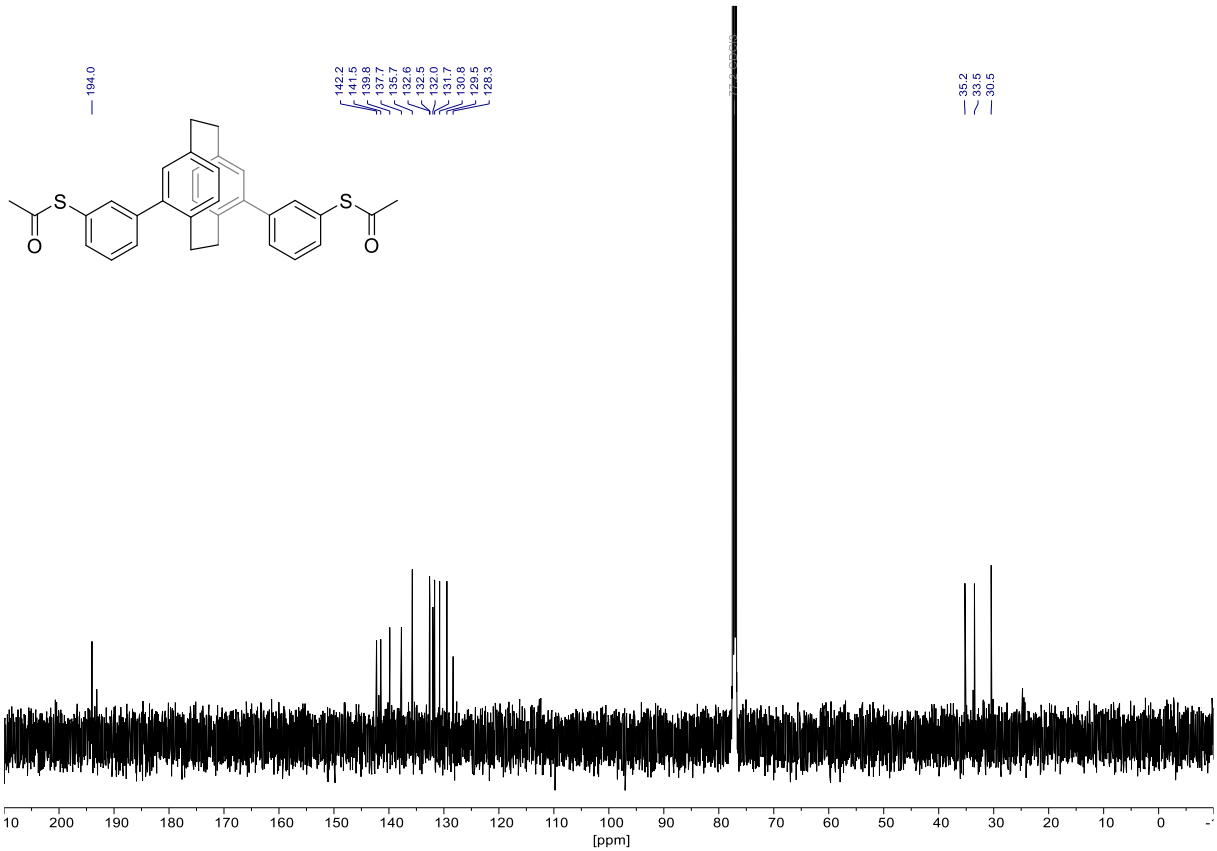

High Resolution Mass Spectrometry Report

Sample Name	**Ksenia Reznikova / KR176**	Instrument	maXis 4G
Comment	10 ug / mL in DCM, analyzed in MeOH+AgNO3 5mM	Method	23 Direct_pos_higher.m

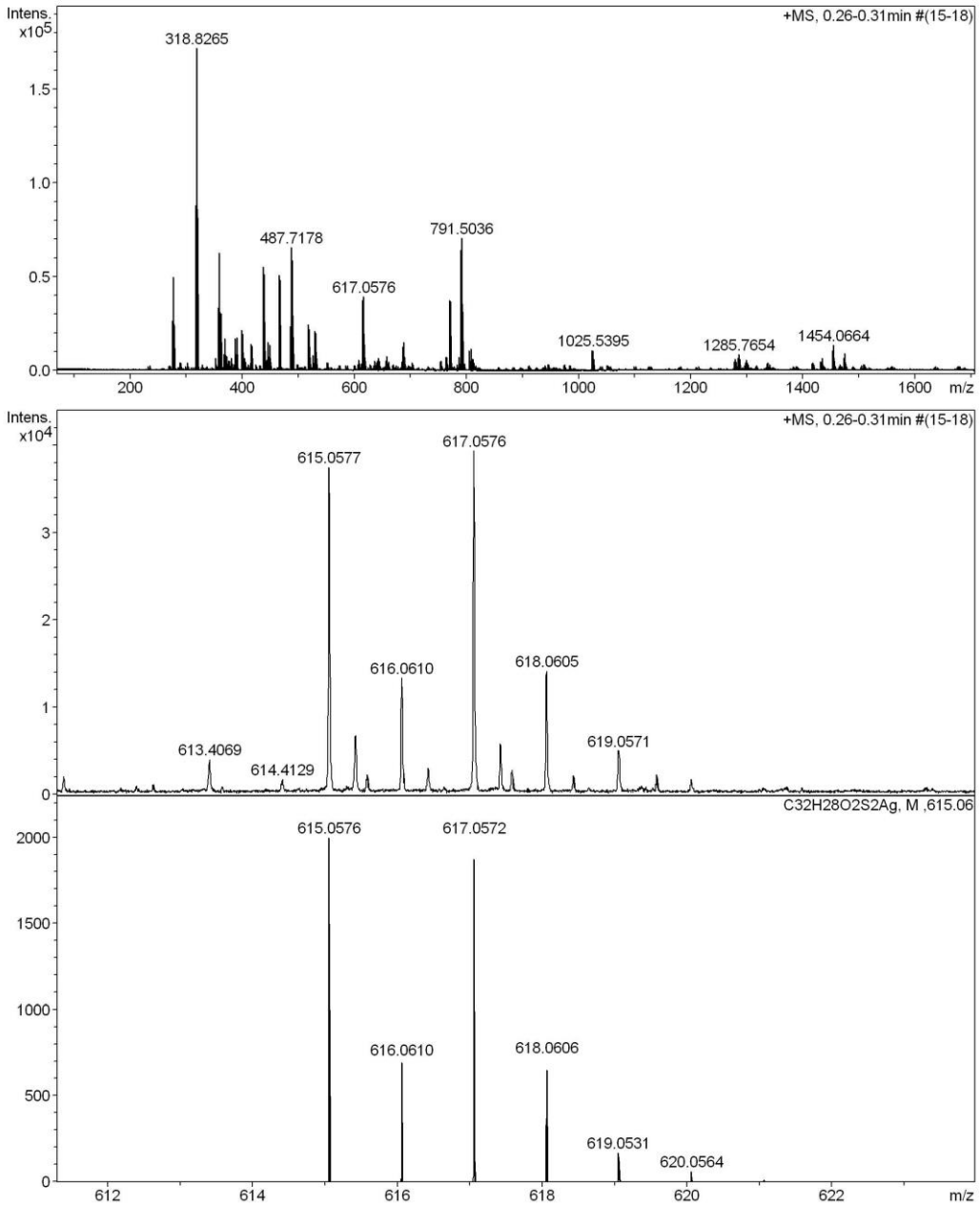

High Resolution Mass Spectrometry Report

Measured m/z vs. theoretical m/z

Meas. m/z	#	Formula	Score	m/z	err [mDa]	err [ppm]	mSigma	rdb	e¯ Conf	z
615.0577	1	C 32 H 28 Ag O 2 S 2	100.00	615.0576	-0.1	-0.2	15.3	18.5	even	1+

Mass list

#	m/z	I %	I
1	275.7992	15.4	26512
2	277.7990	29.0	49862
3	279.7987	14.2	24413
4	316.8265	51.4	88348
5	318.8265	100.0	171959
6	320.8259	47.4	81549
7	353.2684	4.0	6807
8	357.8531	19.5	33557
9	359.8529	36.7	63055
10	361.1314	4.0	6819
11	361.8525	17.7	30482
12	363.1313	4.1	7072
13	367.8236	5.2	9028
14	369.8232	10.0	17274
15	371.8229	4.6	7919
16	377.1469	3.1	5314
17	381.2997	3.8	6591
18	388.1784	10.0	17203
19	389.1628	5.0	8665
20	390.1780	10.3	17783
21	391.1625	4.4	7627
22	399.1103	12.6	21689
23	401.1100	11.4	19679
24	403.8031	4.1	7036
25	415.1050	8.2	14093
26	417.1048	7.7	13228
27	437.1833	32.3	55554
28	438.1865	6.9	11904
29	439.1830	29.9	51439
30	440.1862	6.2	10660
31	444.6914	3.4	5930
32	446.6916	8.8	15122
33	448.6913	8.0	13787
34	465.2141	29.6	50825
35	466.2172	7.2	12390
36	467.2138	28.1	48272
37	468.2171	6.5	11138
38	485.7180	13.8	23713
39	487.7178	38.3	65811
40	489.7174	34.3	58969
41	491.7172	10.7	18361
42	517.2963	14.3	24560
43	518.2999	4.7	8097
44	519.2963	13.0	22326
45	520.2990	4.3	7458
46	526.7442	4.7	8166
47	528.7439	12.4	21365
48	530.7434	11.7	20151
49	532.7430	4.1	6979
50	608.0739	3.4	5845
51	615.0577	21.8	37519
52	615.4221	4.0	6802
53	616.0610	7.8	13376
54	617.0576	22.9	39358
55	617.4258	3.4	5845
56	618.0605	8.2	14162
57	643.4553	4.0	6958
58	656.6103	3.1	5342
59	658.6102	4.5	7730
60	686.1893	7.3	12564
61	688.1898	8.8	15196
62	689.1927	3.2	5437

#	m/z	I %	I
63	690.1901	4.2	7267
64	763.3371	4.3	7432
65	765.3372	4.3	7334
66	769.3550	21.8	37412
67	770.3582	10.3	17688
68	771.3556	21.4	36859
69	772.3586	9.9	16981
70	785.9552	4.2	7207
71	789.5033	37.4	64311
72	790.5061	18.7	32143
73	791.5036	41.1	70609
74	792.5060	18.5	31751
75	793.5064	5.4	9248
76	805.4991	6.3	10839
77	806.5019	3.1	5345
78	807.4992	6.7	11603
79	810.3834	3.6	6199
80	812.3844	3.8	6576
81	1023.5381	6.1	10574
82	1024.5412	3.8	6541
83	1025.5395	6.3	10860
84	1026.5436	3.8	6528
85	1279.5806	3.8	6578
86	1283.7650	4.1	7072
87	1284.7677	3.3	5674
88	1285.7654	5.0	8604
89	1286.7686	3.6	6123
90	1299.7346	3.5	6063
91	1433.9135	3.9	6698
92	1452.0633	6.2	10611
93	1453.0679	5.5	9397
94	1454.0664	8.0	13748
95	1455.0693	6.0	10399
96	1456.0706	3.2	5578
97	1472.2177	3.9	6669
98	1473.2212	3.7	6396
99	1474.2197	5.5	9448
100	1475.2217	4.2	7274

Acquisition Parameter

General	Fore Vacuum	2.54e+000 mBar	High Vacuum	9.65e-008 mBar	Source Type	ESI
	Scan Begin	75 m/z	Scan End	1700 m/z	Ion Polarity	Positive
Source	Set Nebulizer	0.4 Bar	Set Capillary	3600 V	Set Dry Gas	4.0 l/min
	Set Dry Heater	180 °C	Set End Plate Offset	-500 V		
Quadrupole	Set Ion Energy (MS only)	4.0 eV				
Coll. Cell	Collision Energy	8.0 eV	Set Collision Cell RF	500.0 Vpp		
Ion Cooler	Set Ion Cooler Transfer Time	100.0 µs	Set Ion Cooler Pre Pulse Storage Time	18.0 µs		

2. Transport Measurements

2.1 Mechanically Controlled Break Junction

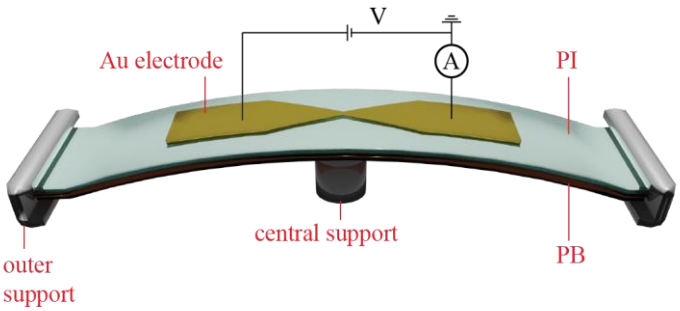

Figure S1: Schematic illustration of the MCBJ setup.

The single-molecule measurements, described in the main text, were carried out with a mechanically controlled break junction. The MCBJ sample consists of a lithographically fabricated gold wire suspended on a flexible substrate made out of phosphor bronze (PB) with an insulating coating of polyimide (PI). The gold wire was defined with electron-beam lithography and evaporated with an electron-beam evaporator with a thickness of 80 nm together with a 3 nm titanium adhesive layer. In a typical room temperature MCBJ measurement, the gold wire is stretched through a three-point bending mechanism with a piezoelectric element and eventually ruptures, forming a nanogap between atomically sharp electrode surfaces for single-molecule characterization. During the breaking of the gold wire, the electrical conductance is recorded with or without the presence of molecules, and the closing of the junction is performed when the contact is broken, as signaled by a conductance below $10^{-6}G_0$. During the successive breaking and making of the gold contacts through the bending/unbending of the substrate, the electrical conductance is monitored, and a large number of "breaking traces" is collected. With a molecule of interest inside the junction, we can determine the single-molecule electrical conductance statistically.

2.2 Fast-Breaking Measurements

In the measurements performed for the PCP molecules, the MCBJ junctions were first characterized without the molecules for reference purposes. After the reference gold measurement, we deposited molecular solutions with concentrations ranging from 1 to 100 μM in CH_2Cl_2 onto the MCBJ samples. The fast-breaking measurements were performed at a constant DC bias voltage with the electrical current recorded by a homemade logarithmic current amplifier. During the fast-breaking measurements, the molecular junctions were continuously opened and closed by the piezoelectric element, creating thousands of conductance breaking traces. The thousands of breaking traces were then plotted together to form a two-dimensional conductance histogram.

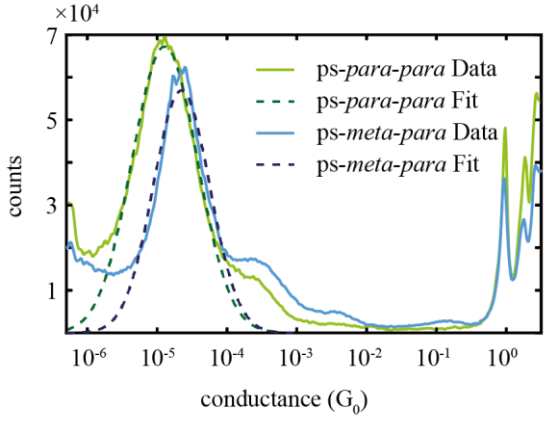

Figure S2: One-dimensional histogram of a fast-breaking measurement of ps-*para-para* and ps-*meta-para* PCP.

The one-dimensional conductance histogram, which is illustrated in Figure S2, was obtained by summing the counts at a fixed conductance level across all displacement values from a two-dimensional conductance vs. displacement histogram (*see* Figure 2). With a log-normal fit, the most probable conductance values for the ps-*para-para* and ps-*meta-para* PCP molecules are $1.3 \times 10^{-5} G_0$ and $2.2 \times 10^{-5} G_0$, respectively.

2.3 Distance-Modulation Measurements

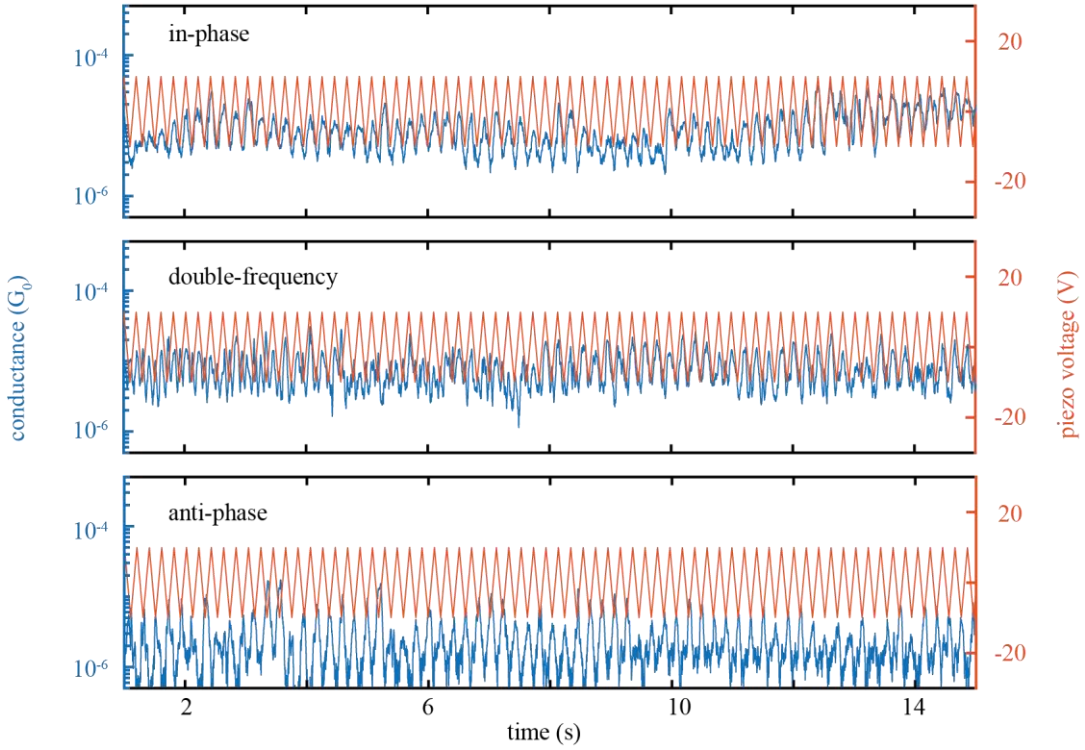

Figure S3: Distance-modulation traces of ps-*para-para* PCP. The blue lines display three different types of conductance measurements, namely in-phase, double frequency, and anti-phase, and the red line displays the voltage applied to the piezoelectric stack. Note that an increase in piezo voltage corresponds to an increase in electrode displacement. The total modulation time of the experiment is 15 seconds.

An additional set of measurements of ps-*para-para* PCP is presented in Figure S3. The modulation traces clearly show in-phase and anti-phase behavior for the whole duration of 15 s. Note that the ascribed double frequency signal changes to the in-phase configuration after around 8 s during the modulation experiment. There are 112 traces in total showing a clear modulation signal in this modulation experiment, and the ratio of each behavior is provided in Figure S4.

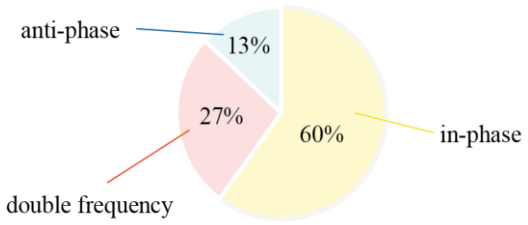

Figure S4: Ratio of phase response behaviors of ps-*para-para* PCP during the distance-modulation experiments.

The ratio between the in-phase, anti-phase, and double-frequency is 60:13:27. The in-phase case is clearly dominating the modulation behavior compared to the anti-phase case. This difference also results in much fewer counts in the negative gauge factor shown in Figure 4a. The scarceness of the anti-phase behavior can be understood by looking at the starting electrode position in the modulation experiment. There, we first opened the junction up to 7.5 Å and then started modulating the junction with an amplitude of 5 Å. The total length of the molecular plateau is about 12.5 Å according to the fast-breaking measurement shown in Figure 2. Although the modulation size in the junction may not directly transform into the deformation of the molecule, we thus expect that the modulation occurs mostly in the strained molecular state. Considering the transmission *vs.* displacement chart for ps-*para-para* PCP shown in Figure 5b and the conductance dip depicted in Figure 3e, the in-phase behavior should be prevalent for a strained molecule.

2.4 Estimation of the Gauge Factor

In the main text, we introduced the gauge factor to quantify the mechano-sensitivity of the molecules. We define it as:

$$\mathrm{GF}(f) \equiv \mathrm{FFT}\left[\log\frac{G}{G_0}\right](f)/\mathrm{FFT}\,[d/d_0](f) \qquad (1)$$

where GF(f) is the frequency-dependent gauge factor, which we evaluate at f=5 Hz. In Eq. (1), FFT is the amplitude of the Fast-Fourier transform, G is the conductance, G_0 is the conductance quantum, d is the electrode displacement estimated from the piezo voltage, and d_0 is the length of the molecule estimated from the most probable molecular length in fast-breaking measurements. Essentially, GF involves a Fast-Fourier transform of the conductance signal on a logarithmic scale and of the electrode displacement on a linear scale. The obtained FFT amplitudes at the driving frequency f of 5 Hz are then taken to define GF by taking the ratio of the two. Note that the sign of GF is fixed by the phase of the signal obtained from the FFT spectra, where in-phase gives a positive GF and anti-phase a negative GF.

For example, if we use a highly mechano-sensitive molecule with mainly anti-phase behavior, we expect to see GF <0, and a large absolute value |GF|≠0 indicates a large conductance change. In the case of a non-mechano-sensitive molecule, such as ps-*meta-para* PCP, |GF| is close to 0, while we find |GF| >1 for the mechano-sensitive ps-*para-para* PCP.

2.5 Stick-Slip Motion in Molecular Junctions

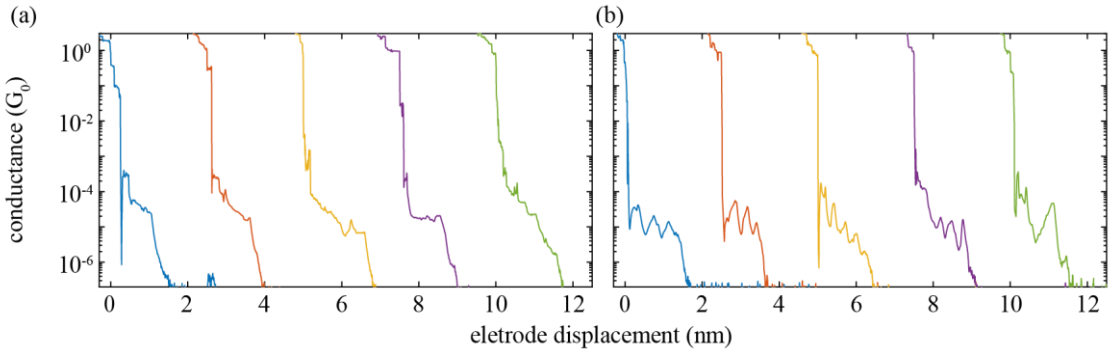

Figure S5: Individual fast-breaking traces for ps-*meta-para* and ps-*para-para* molecules.

In the fast-breaking experiment described in the main text, thousands of breaking traces for ps-*meta-para* and ps-*para-para* molecules were obtained. As suggested by Figure S2, the average conductance value of ps-*meta-para* is slightly larger and exhibits a narrower conductance distribution than those of ps-*para-para*. This is explained by the absence of DQI in the case of ps-*meta-para*. When the individual traces shown in Figure S5 are examined further, it is clear that ps-*para-para* features conductance oscillations during the displacement of electrodes, indicating the presence of DQI. However, oscillations can repeat up to 3 or 4 times instead of the single oscillation expected from crossing a DQI dip. Such a behavior was already observed in the previous experiment with OPE PCP, and we explained it by the stick-slip motion of the molecule in the junction.[7] This stick-slip motion happens, when the molecule is strained sufficiently. As the gold-sulfur connection breaks due to the high strain, the molecule contracts before it establishes a new connection between the sulfur anchor and a nearby electrode gold atom. This process leads to multiple conductance oscillation as observed in the breaking traces. A similar motion can be conceived, if the molecule drags along with it a gold adatom or generally a smaller gold cluster that slides along a macroscopic gold surface. The stick-slip motion is discussed further in the theory section below.

3. Transport Calculations

3.1 DFT Calculation Setup

We describe electronic transport through the PCP-based single-molecule junctions as phase-coherent and elastic in terms of the Landauer scattering theory.[8] The conductance at sufficiently low temperatures simplifies to

$$G = G_0 \tau(E_F), \quad (1)$$

i.e. the product of the energy-dependent transmission function $\tau(E)$, evaluated at the Fermi energy E_F, and the conductance quantum $G_0 = 2e^2/h$. The elastic transmission $\tau(E)$ is computed in a parameter-free approach by combining DFT with NEGF techniques. The established theoretical methods have been discussed in detail previously.[9]

The calculations to obtain the transmission as a function of energy and electrode displacement for the four PCP derivatives comprise the following steps: First, the molecular structures are optimized in the gas phase. Then terminal hydrogens at each sulfur atom are removed, and the molecules are placed between two tetrahedral gold leads. We distinguish "top-top" and "hollow-hollow" junction geometries, where we use either atomically sharp tips, ending with a single Au tip atom for "top-top", or blunt tips for hollow-hollow, where the tip atoms are removed on each side. The resulting junction structures are subsequently optimized by relaxing both the molecule and the four (for top-top geometries) or three (for hollow-hollow geometries) gold atoms that are located at the top of each pyramid. The rest of the gold atoms are fixed in a face-centered cubic lattice configuration. The resulting geometries are displayed in Figure 5a of the main text for the hollow-hollow junction configuration and in Figure S6a for the top-top junction configuration. In the stretching process we separate the gold contacts in steps of 0.1 Å, optimize the geometries as described before, and keep increasing the electrode separation d until the contact ruptures. For compression we proceed in an analogous way until the molecular structure starts to strongly deform. Finally the transmission $\tau(E,d)$ and from Eq. (1) the conductance $G(d)$ are computed for the static geometries within the DFT-NEGF formalism.[9]

The DFT calculations are performed with the quantum chemistry code TURBOMOLE[10], employing the def-SV(P) Gaussian basis set[11] for all atoms and the PBE exchange-correlation functional.[12] Total energies are converged to an accuracy of better than 10^{-8} a.u., while geometries are optimized until the change of the maximum norm of the Cartesian gradient is below 10^{-3} a.u. The transport program[13] that we use for computing the elastic transmission is custom-built and interfaced with TURBOMOLE. For evaluating the transmission function, we employ 16×16 transverse k-points to properly describe the semi-infinite gold electrodes.

3.2 Transmission Maps and Stick-Slip Motion in the Top-Top Configuration

In the main text, we discuss conduction properties of the four PCP molecules immobilized in hollow-hollow junctions. In this part we now focus on a different geometry, namely the behavior of the PCP derivatives in the top-top configuration, see Figure S6a. The conductance and the total energy of DFT are illustrated in Figure S6b for all four PCP derivatives. Considering the example of the ps-*para-para* PCP single-molecule junction, both quantities show pronounced jumps at certain stretching steps during the electrode displacement process. Starting from the initial junction geometry at zero displacement, conductance and total energy grow to a local maximum at 1.5 Å. At this point an anchoring sulfur slips to the next gold atom, see Figure S7a, and the molecule releases the mechanical tension that has been built up due to the mechanical stretching process. An instantaneous decrease of both conductance and energy is observed, restoring the latter to a lower value. After reaching the final tip gold atom, the junction breaks at 5.6 Å, and the molecule snaps back and loses contact to one electrode as the mechanical tension becomes too high, which leads to a sharp drop in the conductance. Molecular contacts based on the other three PCP derivatives show a similar interplay of elastic and plastic stretching stages. The sliding of the anchor group along the surface of the electrode, as presented in Figure S7 and called stick-slip motion, is evident from the experimental data in Figure S5 and has also been observed in our previous work.[7]

In the two-dimensional contour maps of transmission in dependence of energy and electrode displacement, see Figure S6c, sudden geometric rearrangements in the junctions (such as the slipping of the anchor group to a neighboring gold atom) result in a discontinuous distance dependence (for ps-*para-para* PCP at 1.5 Å and 4.6 Å, for ps-*meta-para* PCP at 2.3 Å, for ps-*para-meta* PCP at 3.1 Å and 5.0 Å, and for ps-*meta-meta* PCP at 0.8 Å and 2.4 Å).

A closer look at Figure S6c reveals a similar transport behavior of the top-top molecular junctions compared to the hollow-hollow junctions of Figure 5 in the main text. Again, inside the electronic gap between the HOMO and the LUMO the ps-*para-para* PCP junction shows transmission valleys (blue diagonal traces) with transmission values lower than 10^{-6}, which cause DQI conductance dips. In contrast the ps-*meta-para* PCP junction features a rather constant transmission in the range of about 10^{-3} to 10^{-4}. Different from the observations in the main text, remnants of transmission valleys are faintly visible close to the LUMO for the ps-*para-meta* PCP molecular junction in top-top configuration, further consolidating the hypothesis of the central ps-*para* PCP subunit as origin of the DQI phenomenon. Again, rather uniform transmission values are predicted in the molecule's electronic gap for ps-*meta-meta* PCP as structural analogue with a central ps-*meta* PCP subunit.

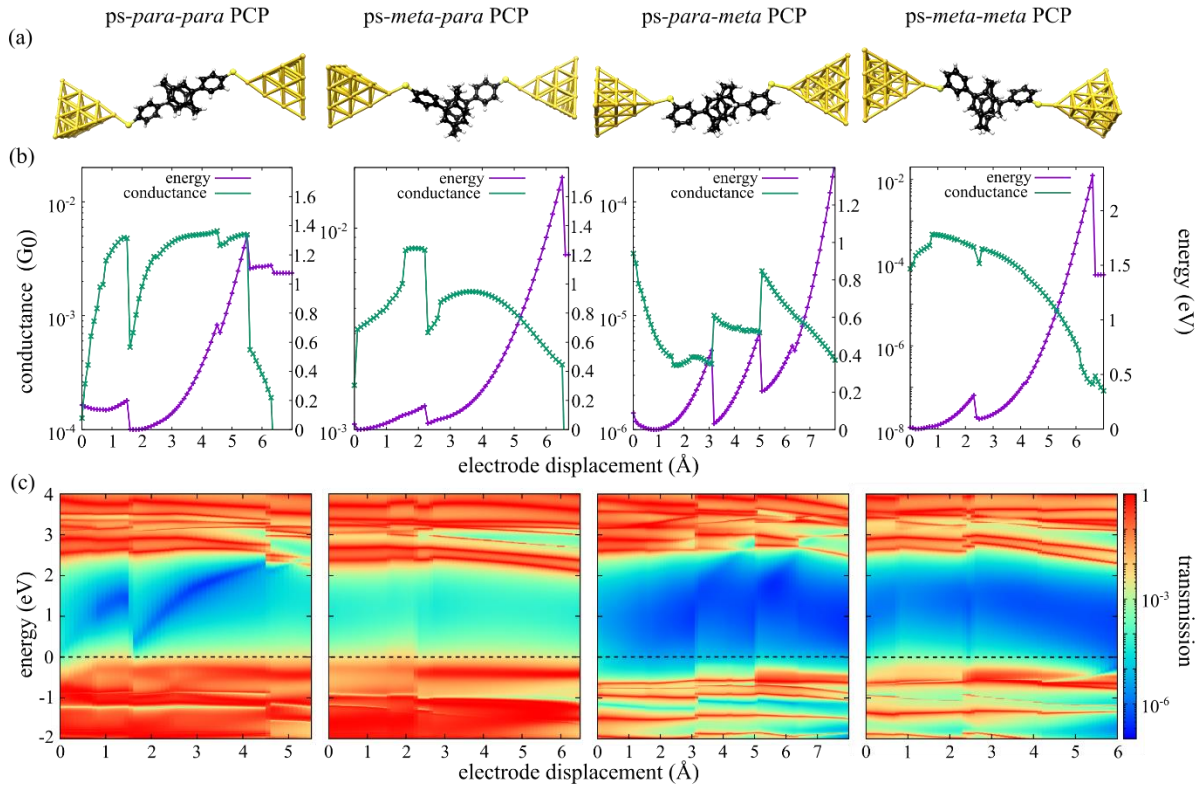

Figure S6: (a) Illustration of the PCP derivatives **1**-**4**, immobilized in top-top junctions between two gold electrodes. (b) Calculated conductance and total energy of the PCP molecular junctions during the gap opening. (c) Transmission maps of the four types of PCP single-molecule junctions. Horizontal red resonances in the maps arise from molecular frontier orbitals. For the ps-*para-para* PCP molecule, an anti-resonance is observed inside the HOMO-LUMO gap that shifts in energy as the displacement is varied. Analogous behavior can be found for the ps-*para-meta* PCP molecule as well, but the effect is masked by the DQI, resulting from the meta coupling at the terminal benzene rings. Tunable DQI effects are neither found in the simulations of ps-*meta-para* PCP junctions nor ps-*meta-meta* PCP junctions with central ps-*meta* PCP systems. The position of the Fermi energy E_F is indicated as a horizontal dashed line in each plot. The conductance curves of panel b are obtained by tracing the transmission along this line.

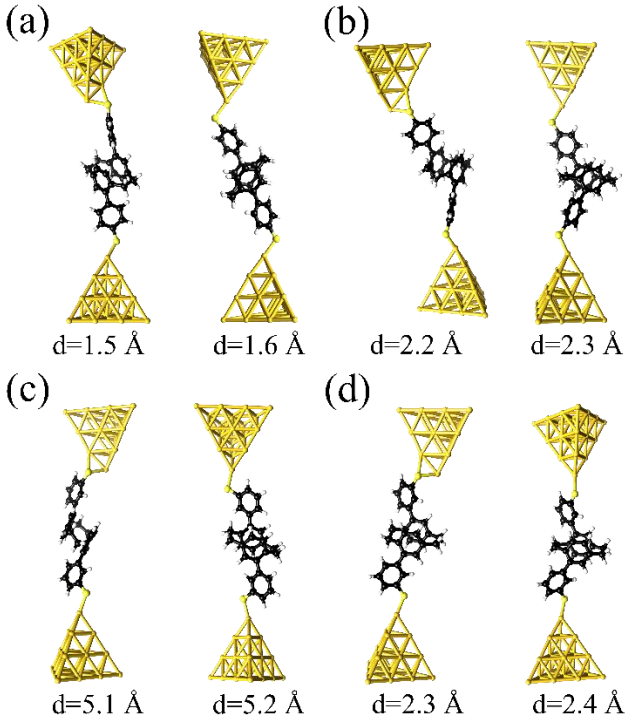

Figure S7: Snapshots illustrating the stick-slip motion of the sulfur anchor group on the gold electrode at different electrode displacements *d* for the (a) ps-*para*-*para*, (b) ps-*meta*-*para*, (c) ps-*para*-*meta*, and (d) ps-*meta*-*meta* PCP molecules.

3.3 Quantum Interference Effects and Symmetry Rules

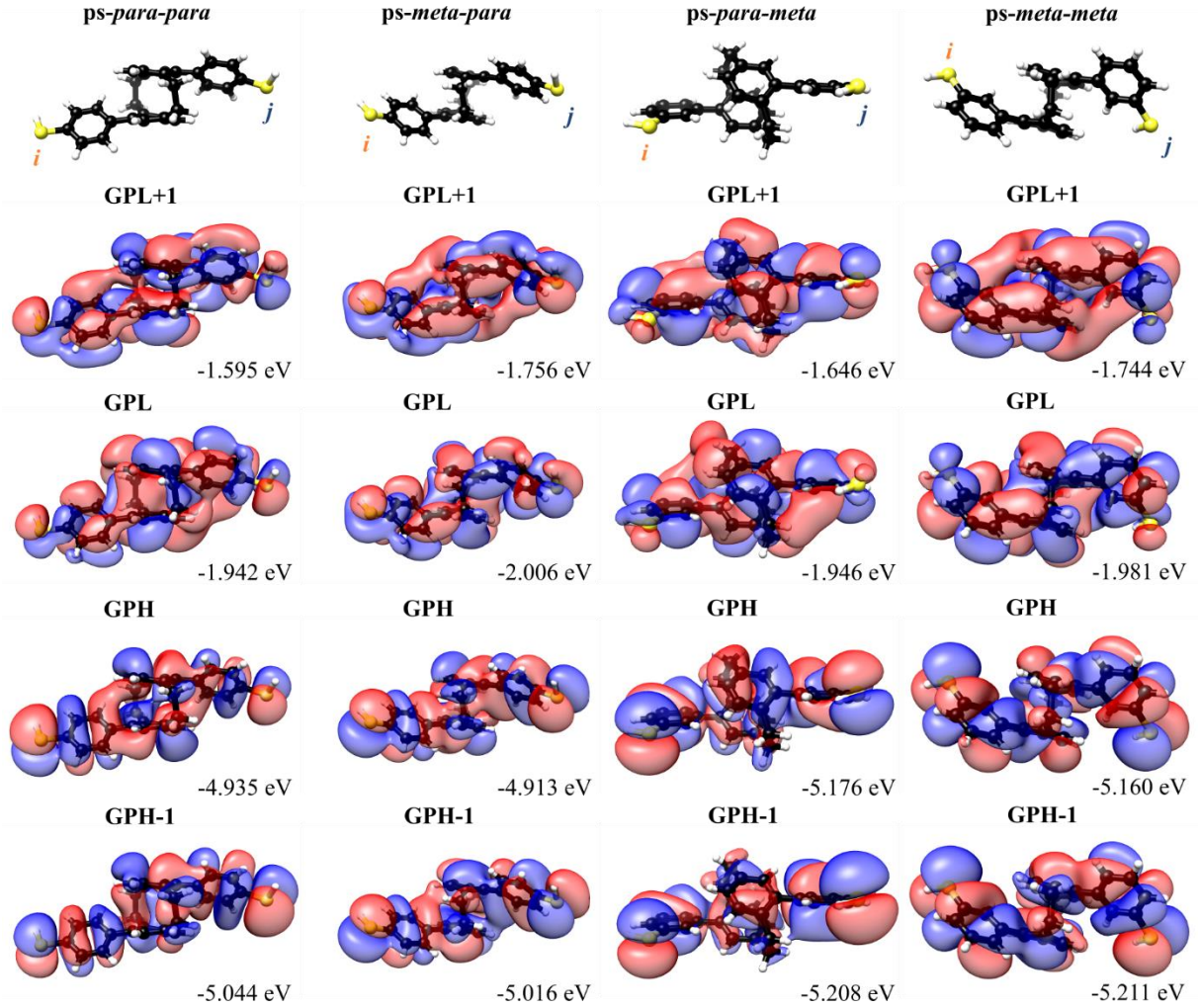

Figure S8: Illustration of frontier molecular orbitals of ps-*para*-*para*, ps-*meta*-*para*, ps-*para*-*meta* and ps-*meta*-*meta* PCP molecules in the gas phase. Shown are the gas phase HOMO (GPH) and gas phase LUMO (GPL), as in Figure 6 of the manuscript, supplemented by the corresponding lower and higher states GPH-1 and GPL+1. The DFT energies of all orbitals are indicated.

We relate the valleys of low transmission in Figures 5 and S6 to DQI effects, resulting from molecular frontier orbital contributions. The appearance or absence of these valleys can be explained by using orbital symmetry rules for the molecules' gas-phase orbitals, which are documented in the literature.[14-16] For off-resonant transport inside the HOMO-LUMO gap, embedding self-energies of the electrodes can be neglected to first approximation. Therefore, the retarded Green's function $G^{\mathrm{r}}_{i\alpha,j\beta}(E)$ that describes the probability amplitude for the propagation of electrons from orbital α at atom i to orbital β at atom j through the molecule can be approximated by the zeroth-order Green's function

$$G^{\mathrm{r},(0)}_{i\alpha,j\beta}(E) = \sum_k \frac{C_{i\alpha,k}C^*_{j\beta,k}}{E+i\eta-\epsilon_k} \tag{2}$$

with the energy ϵ_k of molecular orbital k, its coefficient $C_{i\alpha,k}$ at atom i and atomic orbital α, and a positive infinitesimal broadening parameter η. We identify the sites i and j with the terminal sulfur

atoms of the respective PCPs (see Figure S9). The relation between the transmission and the Green's function

$$\tau(E) \propto \left| G^{\mathrm{r},(0)}_{i\alpha,j\beta}(E) \right|^2 \tag{3}$$

ultimately connects transmission to molecular orbital contributions *k*. In Eq. (3) a sum should be carried out over all orbitals α and β that couple well to the electrodes, and there should be a weighting factor included that depends on this molecule-electrode coupling. For simplicity and under the assumption that the energy *E* is located between the HOMO energy ϵ_{HOMO} and the LUMO energy ϵ_{LUMO}, we reduce the Green's function in Eq. (2) to the largest terms and thus only consider the HOMO and LUMO contributions

$$G^{\mathrm{r},(0)}_{i\alpha,j\beta}(E) \approx \frac{C_{i\alpha,\mathrm{HOMO}} C^*_{j\beta,\mathrm{HOMO}}}{E+i\eta-\epsilon_{\mathrm{HOMO}}} + \frac{C_{i\alpha,\mathrm{LUMO}} C^*_{j\beta,\mathrm{LUMO}}}{E+i\eta-\epsilon_{\mathrm{LUMO}}}. \tag{4}$$

For a full description of the transmission behavior further orbital contributions *k* may need to be taken into account[16], but Eq. (4) still allows for a qualitative explanation of the occurrence or absence of DQI in the case of the studied PCP systems. We will omit the atomic orbital indices α and β in Eqs. (2)-(4) in the following and not specify them further, similar to the presentation in the paper. They will simply be of the form of the HOMO and LUMO wavefunctions at the atoms *i* and *j*. It is important though that the orbital characters of HOMO and LUMO wavefunctions are of compatible character in order to interfere as given in Eq. (4). Figure S8 reveals that this is the case here, i.e. all of the relevant HOMOs and LUMOs exhibit the same π-character and spatial orientation at the respective terminal sulfur atoms for each of the four PCP derivatives. The form of the Green's function in Eq. (4) combined with Eq. (3) allows to draw the following conclusions[12,13]: First, the products of the orbital coefficients $C_{i\mathrm{HOMO}} C^*_{j\mathrm{HOMO}}$ of the HOMO and $C_{i\mathrm{LUMO}} C^*_{j\mathrm{LUMO}}$ of the LUMO need to be of decent size in order to contribute to the transmission. For this reason, the weights of HOMO and LUMO wave functions need to be sufficiently large on the anchoring atoms *i* and *j*, meaning that these are delocalized orbitals. Second, the parities of the molecule's HOMO and LUMO need to be different ($\mathrm{sign}(C_{i\mathrm{HOMO}} C^*_{j\mathrm{HOMO}}) = -\mathrm{sign}(C_{i\mathrm{LUMO}} C^*_{j\mathrm{LUMO}})$) in order to achieve high transmission, as in this case the terms in Eq. (4) add up. If the parities of HOMO and LUMO are the same instead, the two terms cancel each other inside the gap, and DQI occurs, resulting in a low transmission. Figure S8 shows relevant frontier molecular orbitals and their energies, from which orbital weights on terminal sulfurs as well as their parity can be inferred. The quantities are needed to rationalize the transport behavior in Figure 5 of the main text as well as Figure S6 in terms of the orbital symmetry rules.

3.4 Transmission Eigenchannels

Figure S9 visualizes the wave function of those left-incoming transmission eigenchannels with the highest transmission for each of the four studied PCP isomers at the Fermi energy and at a particular

electrode separation *d*. We see that the amplitude of the eigenchannels decays along the propagation direction inside the molecules, as expected in an off-resonant transport situation.

The spatial distribution of the wave function is quite similar for all four molecules, exhibiting a high weight on the molecular deck that is directly connected through a sulfur anchor to the left electrode and a low weight on the molecular deck that is directly connected to the right electrode. Note the low weight of the wave function on the ethylene braces of the central paracyclophane units. It indicates that they do not contribute to the phase-coherent electronic transmission through the PCP molecules at E_F.

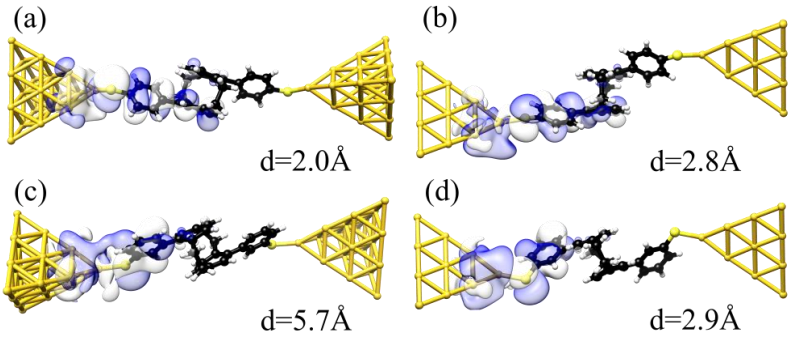

Figure S9: Illustration of the wave function of the most transparent left-incoming transmission eigenchannel, evaluated at the Fermi energy E_F, for electron transport through (a) ps-*para-para*, (b) ps-*meta-para*, (c) ps-*para-meta*, and (d) ps-*meta-meta* PCP molecules connected to gold electrodes. The selected electrode displacement *d* is indicated separately for each junction.

4. References

(1) Duncan, K. D.; Fang, R.; Yuan, J.; Chu, R. K.; Dey, S. K.; Burnum-Johnson, K. E.; Lanekoff, I. Quantitative Mass Spectrometry Imaging of Prostaglandins as Silver Ion Adducts with Nanospray Desorption Electrospray Ionization. *Anal. Chem.* **2018**, *90* (12), 7246–7252. https://doi.org/10.1021/acs.analchem.8b00350.

(2) Munakata, M.; Wu, L. P.; Sugimoto, K.; Kuroda-Sowa, T.; Maekawa, M.; Suenaga, Y.; Maeno, N.; Fujita, M. Silver(I) Complex Assemblies with Nonplanar Aromatic Compounds. *Inorg. Chem.* **1999**, *38* (25), 5674–5680. https://doi.org/10.1021/ic990391m.

(3) Vorontsova, N. V.; Rozenberg, V. I.; Sergeeva, E. V.; Vorontsov, E. V.; Starikova, Z. A.; Lyssenko, K. A.; Hopf, H. Symmetrically Tetrasubstituted [2.2]Paracyclophanes: Their Systematization and Regioselective Synthesis of Several Types of Bis-Bifunctional Derivatives by Double Electrophilic Substitution. *Chem. – Eur. J.* **2008**, *14* (15), 4600–4617. https://doi.org/10.1002/chem.200701683.

(4) Søndergaard, R.; Krebs, F. C. The Challenge of Synthesizing Oligomers for Molecular Wires. *Polymers* **2011**, *3* (1), 545–557. https://doi.org/10.3390/polym3010545.

(5) Kahrs, C.; Wickleder, M. S.; Christoffers, J. Biphenyl Sulfonic and Disulfonic Acids with Perfluorinated Alkyl Residues. *Eur. J. Org. Chem.* **2018**, *2018* (41), 5754–5762. https://doi.org/10.1002/ejoc.201800882.

(6) Jevric, M.; Petersen, A. U.; Mansø, M.; Madsen, A. Ø.; Nielsen, M. B. Bismuth(III)-Promoted Acetylation of Thio-ethers into Thioacetates: Bismuth(III)-Promoted Acetylation of Thioethers into Thioacetates. *Eur. J. Org. Chem.* **2015**, *2015* (21), 4675–4688. https://doi.org/10.1002/ejoc.201500420.

(7) Stefani, D.; Weiland, K. J.; Skripnik, M.; Hsu, C.; Perrin, M. L.; Mayor, M.; Pauly, F.; van der Zant, H. S. J. Large Conductance Variations in a Mechanosensitive Single-Molecule Junction. *Nano Lett.* **2018**, *18* (9), 5981–5988. https://doi.org/10.1021/acs.nanolett.8b02810.

(8) Cuevas, J. C.; Scheer, E. *Molecular Electronics : An Introduction to Theory and Experiment*, 2nd ed.; World Scientific: Singapore, 2017.

(9) Pauly, F.; Viljas, J. K.; Huniar, U.; Häfner, M.; Wohlthat, S.; Bürkle, M.; Cuevas, J. C.; Schön, G. Cluster-Based Density-Functional Approach to Quantum Transport through Molecular and Atomic Contacts. *New J. Phys.* **2008**, *10* (12), 125019. https://doi.org/10.1088/1367-2630/10/12/125019.
(10) Ahlrichs, R.; Bär, M.; Häser, M.; Horn, H.; Kölmel, C. Electronic Structure Calculations on Workstation Computers: The Program System Turbomole. *Chem. Phys. Lett.* **1989**, *162* (3), 165–169. https://doi.org/10.1016/0009-2614(89)85118-8.
(11) Schäfer, A.; Horn, H.; Ahlrichs, R. Fully Optimized Contracted Gaussian Basis Sets for Atoms Li to Kr. *J. Chem. Phys.* **1992**, *97* (4), 2571–2577. https://doi.org/10.1063/1.463096.
(12) Perdew, J. P.; Burke, K.; Ernzerhof, M. Generalized Gradient Approximation Made Simple. *Phys. Rev. Lett.* **1996**, *77* (18), 3865–3868. https://doi.org/10.1103/PhysRevLett.77.3865.
(13) Bürkle, M.; Viljas, J. K.; Vonlanthen, D.; Mishchenko, A.; Schön, G.; Mayor, M.; Wandlowski, T.; Pauly, F. Conduction Mechanisms in Biphenyl Dithiol Single-Molecule Junctions. *Phys. Rev. B* **2012**, *85* (7), 075417. https://doi.org/10.1103/PhysRevB.85.075417.
(14) Yoshizawa, K.; Tada, T.; Staykov, A. Orbital Views of the Electron Transport in Molecular Devices. *J. Am. Chem. Soc.* **2008**, *130* (29), 9406–9413. https://doi.org/10.1021/ja800638t.
(15) Nozaki, D.; Lucke, A.; Schmidt, W. G. Molecular Orbital Rule for Quantum Interference in Weakly Coupled Dimers: Low-Energy Giant Conductivity Switching Induced by Orbital Level Crossing. *J. Phys. Chem. Lett.* **2017**, No. 8 (4), 727–732. https://doi.org/10.1021/acs.jpclett.6b02989.
(16) Tsuji, Y.; Yoshizawa, K. Frontier Orbital Perspective for Quantum Interference in Alternant and Nonalternant Hydrocarbons. *J. Phys. Chem. C* **2017**, *121* (17), 9621–9626. https://doi.org/10.1021/acs.jpcc.7b02274.